



New strategies to develop High-Efficiency Lead-Free wide bandgap perovskite solar cells



Padmini Pandey ^a, SungWon Cho ^b, Shuzi Hayase ^c, Jung Sang Cho ^{d,*}, Dong-Won Kang ^{a,b,*}

^a Department of Energy Systems Engineering, Chung-Ang University, 84 Heukseok-ro, Dongjak-gu, Seoul 06974, South Korea

^b Department of Smart City, Chung-Ang University, 84 Heukseok-ro, Dongjak-gu, Seoul 06974, South Korea

^c Info-Powered Energy System Research Center, The University of Electro-Communications, 1-5-1 Chofugaoka, Chofu, Tokyo 182-8585, Japan

^d Department of Engineering Chemistry, Chungbuk National University, 1 Chungdae-Ro, Seowon-Gu, Cheongju-si, Chungbuk 361-763, South Korea

ARTICLE INFO

Keywords:

Pb-free
Sn
Wide bandgap
Defect passivation
Perovskite solar cells

ABSTRACT

Over the past decade, the world has witnessed tremendous achievement in power conversion efficiency (PCE) enhancement for Pb-perovskite solar cells (PSCs). However, spectral loss limits the performance, which can be overcome with tandem solar cells (TSCs) and hence with excellent optoelectronic properties and bandgap tunability Pb-perovskites have been widely used as front/rear sub-cells in TSCs, where variable bandgap sub-cells can utilize maximum spectral radiations. Though the operational instability issue has been well controlled by structural optimizations, yet Pb toxicity is a major challenge in commercializing Pb-PSCs. To resolve the issue of toxicity, Pb-free perovskites have gained immense consideration, especially Sn^{2+} having similar physical properties to Pb^{2+} and non-toxic feature of Sn^{2+} , Ge^{2+} , Bi^{3+} , or Sb^{3+} perovskites. In TSCs, the wide bandgap (WBG \geq 1.6 eV) sub-cell plays a critical role in harnessing shorter wavelength photons and is responsible to achieve high V_{oc} . To nurture Pb-free all-PTSC technology, it is urgent to develop high-performance Pb-free WBG PSCs. To understand the seriousness herein, this review focus on the existing challenges in Pb-free WBG PSCs and discuss new strategies that have been implemented with state-of-the art fabrication techniques to enhance device performance. By discussing the issues of trap densities, defects formation, bandgap mismatching, V_{oc} deficits, and poor stability, we focused on the strategies to overcome these issues through compositional engineering, and defect passivation via additive and interfacial engineering. In conclusive remarks, we discussed our viewpoint with innovative ideas that can be applied to collectively focus on this area to achieve high-performance Pb-free WBG PSCs.

1. Introduction

The world is facing issues of environmental pollution, the annihilation of species, and global warming due to diverse transformations in habitats. There is an urgent need of minimizing the usage of fossil fuels. For long-term energy requirements, the utilization of renewable energy is promising to address these issues [1]. Of various renewable energies, solar energy is the most abundant and significant for next-generation technology [2]. Despite having high efficiency in silicon-based technology [3], one of the major challenges is the processing cost of these devices and their limited availability. Organic-inorganic halide perovskites (OIHPs) are promising candidates and made rapid progress over the past decades, due to wide-range bandgap tunability, ease in dopant-

induced optoelectronic modification, longer diffusion length, and high carrier mobility. Perovskite solar cells (PSCs) already reached the certified power conversion efficiency (PCE) of 25.7% [4], not much far from the Shockley-Queisser (SQ) limit of 33%. However, the unutilized solar energy is ascribed as spectral loss due to the limited optical response of photo-absorbers. Single-junction (SJ) solar cells are incapable to avoid the excess thermalization loss and cannot exploit photons with energy less than the bandgap (E_g) and hence suffer from the limited optical response. The excess non-radiative thermal energy loss and photons with lower energies than E_g remain unutilized (Fig. 1(a)) [5]. For further efficiency enhancement, tandem solar cells (TSCs) have been developed, which can harness maximum photons in a broad spectral range. TSCs can efficiently harvest solar energy, where shorter

* Corresponding authors at: Department of Energy Systems Engineering, Chung-Ang University, 84 Heukseok-ro, Dongjak-gu, Seoul 06974, South Korea (D.-W. Kang), Department of Engineering Chemistry, Chungbuk National University, 1 Chungdae-Ro, Seowon-Gu, Cheongju-si, Chungbuk 361-763, South Korea (J. S. Cho).

E-mail addresses: jscho@cbnu.ac.kr (J. Sang Cho), kangdwn@cau.ac.kr (D.-W. Kang).

wavelength photons get absorbed by the front wide-bandgap (WBG, e.g. 1.6–2.3 eV) sub-cell, and longer wavelength photons get absorbed by the rear narrow-bandgap (NBG, e.g. 1–1.3 eV) sub-cell (Fig. 1(b)) [5–9]. This allows harnessing of maximum photons in the solar spectrum. TSCs are categorized into two types i.e., four-terminal (4T-TSCs) and two-terminal monolithically integrated TSCs (2T-TSCs) (Fig. 1(c-d)).

4T-TSCs are further classified into two configurations: mechanically stacked 4T-TSC and spectrally split 4T-TSCs. They are fabricated by coupling two independent sub-cells, and the device configuration undergoes optical losses, fabrication complexity and involvement of multiple transparent electrodes leading to higher device cost [10,11]. 2T-TSCs are also categorized into two configurations, single transparent electrode based sequential fabrication of front and rear-sub-cell coupled with an interconnecting layer (ICL) (Fig. 1(d)) and mechanically stacked 2T-TSCs with multiple transparent conducting oxide (TCO) electrodes. The overall power of 4T-TSCs is the summation of efficiencies of sub-cells, hence a wide range of E_g can be chosen for the front sub-cell (Fig. 1(e)). While the open circuit voltage (V_{oc}) in 2T-TSCs is the summation of both sub-cells, there is a limitation in short circuit current density (J_{sc}) due to lower values of both sub-cells. Hence the selection of photo-absorbers with appropriate E_g needs to be strictly followed to get maximized J_{sc} and PCE in 2T-TSCs (Fig. 1(f)). In Fig. 1(e-f), the black and red dotted line represents c-Si/CIGS ($E_g \sim 1.1$ eV) and perovskite ($E_g \sim 1.2$ –1.27 eV) as rear sub-cells, respectively, that could ideally

couple with OIHPs front-cell in a range of 1.55–1.9 eV bandgap to harvest theoretically limiting efficiency of 44% in both 4T and 2T-TSCs [9].

Typically, WBG front sub-cells are important to achieve high V_{oc} in TSCs and are currently a part of extensive research to develop high quality WBG perovskites. Electrical tolerance of OIHPs is appropriate for TSCs, which can effectively reduce defect densities arising from surface and bulk defects, induced by the lattice disparity between front/rear sub-cells. There is sufficient room to build high efficiency all-perovskite TSCs in terms of optoelectronic properties modulation, processibility, and cost effectiveness. However, structural instability and performance degradation over time due to moisture penetration and Pb-toxicity are the major challenges (as discussed in section 2) that should be overcome before its commercialization [12]. Though considerable progress has been pursued in handling Pb leakage and instability through encapsulations and recycling of Pb, achieving competent, highly stable, and non-toxic OIHPs has become the next essential requirement for eco-friendly PSCs [13,14]. To reduce the usage of Pb in OIHPs the approaches of partial or complete replacement of Pb^{2+} with specific non-hazardous cations such as Sn^{2+} , Ge^{2+} , Bi^{3+} , or Sb^{3+} , are of great interest [15]. Partial replacement of Pb^{2+} with Sn^{2+} forms alloy, developing the concept of bowing effect [16], i.e., the E_g of Pb-Sn alloy (e.g. $MASn_0.5Pb_0.5I_3$, $E_g \sim 1.18$ eV) is narrower than the E_g of both end perovskites, e.g. $MAPbI_3$ ($E_g \sim 1.6$ eV) and $MASnI_3$ ($E_g \sim 1.3$ eV), which is

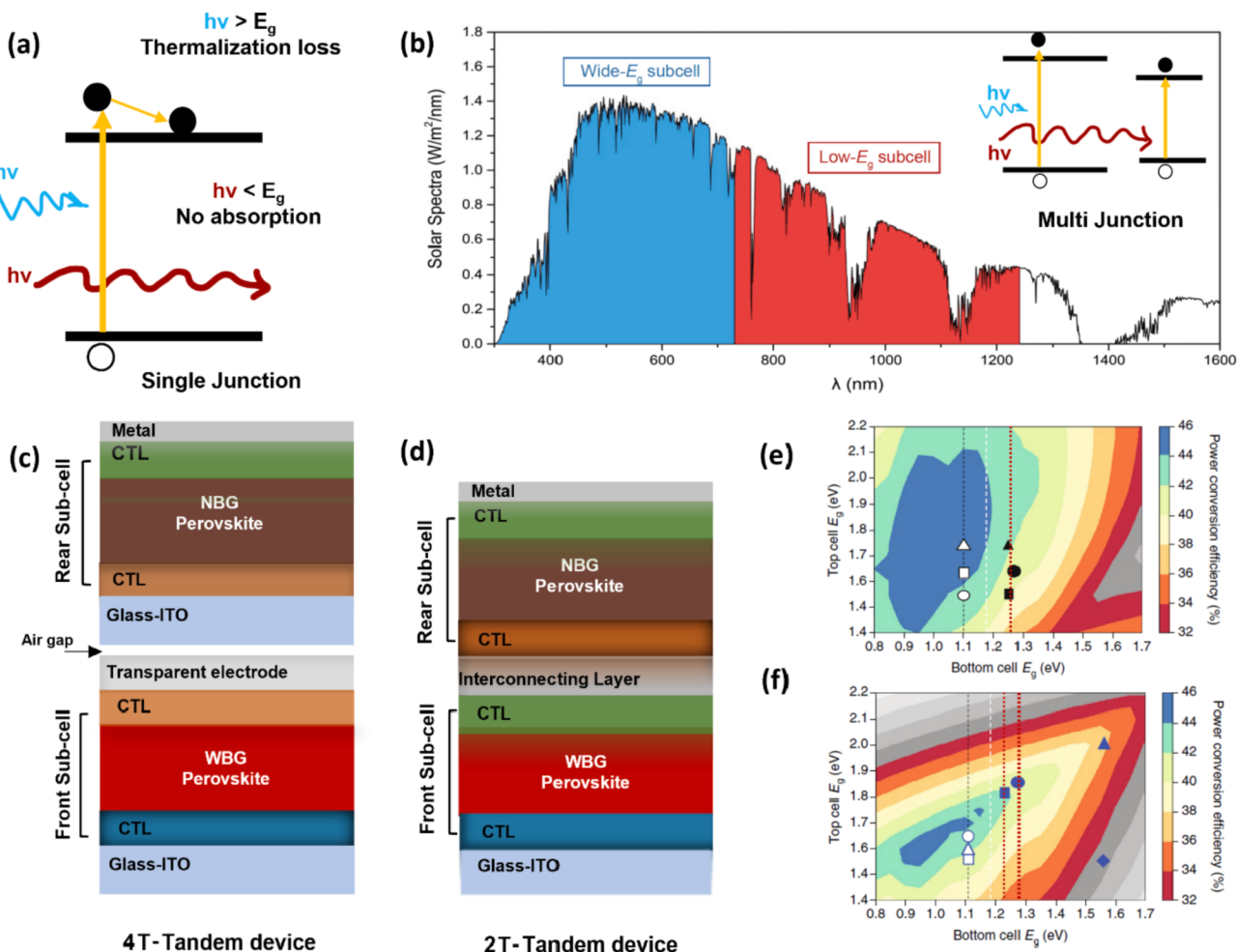


Fig. 1. (a) Photon absorption and thermal loss in single-junction PSC (b) Solar spectrum indicating the spectral zone over which two semiconductors could absorb photons in multijunction PSCs (TSCs) [5]. Reproduced with permission from Springer Nature. Copyright (2020). Graphical representation (c, d) for four-terminal (4T-TSCs) and two-terminal (2T-TSCs) (e-f) theoretical PCE limits in 4T-TSCs and 2T-TSCs, where black dotted line represents c-Si bandgap, and white dotted line represents the lowest accessible bandgap in OIHPs. Red line indicates the rear sub-cell bandgap for OIHPs, and black and blue solid symbols depict OIHPs WBG front sub-cell in all-perovskite TSCs. Reproduced with permission from Springer Nature. Copyright (2018) [9].

due to nonlinear dependency on chemical compositions [16,17].

Sn-OIHPS as a replacement for Pb in PSCs widely used as NBG absorbers and enormous efforts have been made to date for PCE enhancement. However, to promote environmentally benign next-generation Pb-free all-perovskite TSCs, it is very crucial to develop high efficiency Pb-free WBG PSCs. The technological development in this field is very recent and needs more attention to achieve high PCEs. The replacement of Pb^{2+} with Sn^{2+} , Ge^{2+} , Bi^{3+} or Sb^{3+} may overcome the toxicity issue, although it is not the only point to focus on developing high efficiency device. As it is a part of recent technology, there are several other issues involved that hamper the PCE in these perovskites (as discussed in section 3) such as faster crystallization that results in poor film morphology, surface defects, and moisture penetration, causing instability, trap densities, recombinations at the interfaces, poor band alignments, deprived J_{sc} and V_{oc} deficit.

To identify the seriousness and urgency of developing high efficiency Pb-free WBG PSCs, the present review aims to discuss associated challenges and possible strategies adopted to overcome the issues and achieve high performance in Pb-free WBG PSCs. Section 3 deals with major challenges associated and later in section 4 we have provided the state-of-the-art processing and grain engineering techniques, defect passivation strategies through compositional modifications and additive engineering, V_{oc} and J_{sc} enhancement through modifications at perovskite/charge transport layer (CTL) interfaces for efficient charge injection and band alignment and so on. To immediately pursue research in developing high efficiency Pb-free WBG PSCs, we have systematically discussed several strategies that have been established so far with pioneering achievements. The final section 5 deals with the conclusion and our perspective on new ideas and engineering strategies that extend the prospect of designing and developing high performance Pb-free WBG PSCs for next-generation Pb-free all perovskite TSCs technology.

2. Issues related to Pb-based PSCs

2.1. Stability issue

Issues associated with PCE deterioration over the long run are mainly associated with structural instability and moisture-induced damage in Pb-OIHPS [18]. Long-term exposure to oxygen results in the formation of

superoxide (O_2^-) which fits into the iodine vacancies V_I . It tends to deprotonate $CH_3NH_3^+$ ion and dissociates the compound, which leads to oxygen induced degradation [18]. Photo/thermal decomposition inclining to irreversible degradation of organic species generates PbI_2 rich surface, which further decomposes to Pb_0 and I_2 (Fig. 2(a)). It is responsible for structural degradation and limits the operational stability of Pb-OIHPS [19]. Electronic trap density, crystallographic defects, and grain boundaries originate during film fabrication, which are accountable for moisture-induced degradations (Fig. 2(b)). Interstitial/vacancy defects with low formation energies result in ion migration, and light induced ion migration (Fig. 2(c)) tends to cause phase segregation and formation of I/Br^- rich phases. Hence these issues collectively reduce the device performance over time [20–22].

2.2. Pb toxicity issue

Pb-preursors in PSCs are responsible to pollute the environment and cause severe health damage. Pb^{2+} can mimic Ca^{2+} and Zn^{2+} cations and accumulate in the nervous system which causes neurological disorders [23]. To suppress the environmental pollution, recycling and device encapsulations are required. Perhaps these strategies are not enough to fully ignore the risk of Pb leakage. Considering the above issue, replacement of Pb^{2+} cation in OIHPS is a matter of constant research to develop Pb-free OIHPS with identical optoelectronic features for SJ and TSCs [24,25]. It is crucial to make advances in Pb-free WBG OIHPS for perovskite TSCs.

3. Challenges towards efficiency enhancement in Pb-free WBG PSCs

For developing stable and non-toxic OIHPS comparable to Pb-OIHPS, it is crucial to focus on its intrinsic properties, such as $6s^26p^0$ electronic configuration state of Pb^{2+} cation and defect tolerance that relates to 6 s^2 lone pair. Strong spin-orbit coupling is responsible for its exceptional electronic properties [26]. The similarity in chemical characteristics, resemblance in electronic configuration, equivalent ionic radii of Sn^{2+} (118 pm) with Pb^{2+} (119 pm), and lone pair of 5 s^2 outermost orbital, bring uniqueness to the optoelectronic properties of Sn perovskite, which makes it the most promising alternative of Pb to develop of Pb-

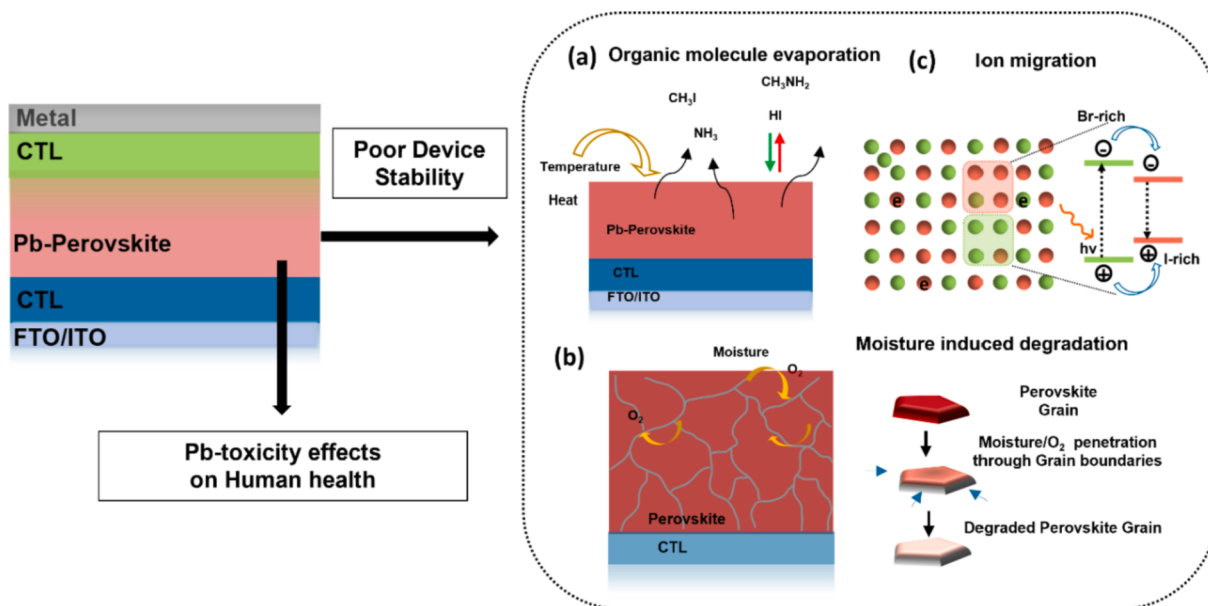


Fig. 2. Illustration of Pb PSC, associated issues with Pb-OIHPS: poor device stability and Pb-toxicity. (a) Thermal and photodegradation as shown in the decomposition processes involve the irreversible decomposition of organic species into volatile components, (b) moisture penetration in perovskite through grain boundaries leads to degradation of grains, and (c) ion migration process and light-induced phase separations in mixed halide perovskites.

free WBG PSCs [27,28]. In 2014, Kanatzidis and co-workers demonstrated the initial PCE of 5.73% for WBG Sn-based PSCs on FTO/TiO₂/perovskite/spiro-OMeTAD/Au n-i-p device architecture [29] (Fig. 3). Subsequently several efforts were made to improve the device performance in n-i-p architecture. However, no substantial improvement in PCE for WBG PSCs has been observed for n-i-p device structure, which may relate to poor interfacial contacts and band alignments between perovskite/CTL. It leads to poor charge injection and inadequate carrier transport, resulting in enhanced hysteresis in device with poor efficiency. Even the carbon-based PSCs are promising for the next-generation technology, whereby efforts were made to enhance PCEs in Pb-free WBG carbon PSCs as well. However, the existence of carbon with limited optical response restricts the light harvesting in carbon PSCs. Song et al., [30] reported PCE ~ 5.4% for WBG GA_{0.2}FA_{0.8}SnI₃: EDAL₂(15%) ($E_g = 1.61$ eV) at mesoporous architecture FTO/TiO₂/perovskite/Al₂O₃/ITO. Furthermore, Zhang et al., 2016 investigated the p-i-n device architecture for Sn-based WBG perovskite constructed on ITO/PEDOT:PSS/FASnI₂Br/C₆₀/Ca/Al structure [31]. Although the initial PCE at inverted device structure was very poor approx. 1.72%, yet over the years with multiple efforts the PCE in Sn WBG PSCs reached a respectably high value of 11.17% in 2022 [32] (Fig. 3).

Likewise, Ge also considered as an alternative in Pb-free PSCs. However, due to small ionic radii of Ge²⁺ (73 pm) and low solubility of precursors, it generated poor device performance [12]. Another alternative to reduce Pb-toxicity is heterovalent substitution at B site with trivalent cations (Bi³⁺ and Sb³⁺) which modify the crystal structure in OIHPs. The direct replacement of Pb²⁺ with trivalent cation alters the 3D ABX₃ structure to A₃B₂X₉. For instance, Bi-perovskites crystallize in a 0D structure in Cs₃Bi₂I₉ with an indirect E_g of 1.9–2.0 eV and binding energy of approx. 270 meV. Sb perovskites typically exist in two derivatives i.e., 0D structure with isolated face shared [Sb₂X₉]⁻³ dimers and 2D structure with corner shared [SbX₆]⁻³ sheets wherein A-Sb-Xs, A⁺ = Rb⁺ or K⁺ inherently form a layered structure. Pb-free halide double perovskite is another alternative to reduce Pb toxicity, as a transmutation of Pb²⁺ replacement with one B⁺ (Ag⁺) monovalent cation and one B³⁺ (Bi³⁺) trivalent cation forms Cs₂AgBiBr₆ double perovskite ($E_g \sim 2$ –2.3 eV).

The unsatisfactory device performance is expected to be caused due to the existence of defects, instability, and poor band alignments that need to get resolved to achieve high performance Pb-free WBG PSCs. Fig. 4(a) depicts the issues associated with Pb-free WBG PSCs. The crystallization process in Pb-free WBG perovskites is faster as compared to the Pb counterpart. For instance, due to the comparatively high energy of Sn 5p atomic orbitals, Lewis acidity in Sn²⁺ is higher, which leads to a fast reaction rate. Consequently, fast crystallization results in the formation of poor perovskite film with smaller grain size (Fig. 4(a)). In addition, non-uniformity and random crystal orientation are collectively responsible for the surface defects. Even the existence of deep

traps and unexpected recombinations in these perovskites affect the charge transport properties and worsen the device efficiency. Especially for Sn-OIHPs, their growth conditions lie in a narrow chemical range [33], which needs to be controlled precisely during synthesis. Intrinsic low ionization potential in Sn-OIHPs is responsible for Sn vacancies and iodine defects, which relates to self p-doping that increases the hole concentration. Furthermore, oxidation of Sn²⁺ promoted by local I-rich environment generates deep trap states. The charge distribution studies suggest that Sn 5s and I 5p antibonding orbitals contribute to valence band maxima (VBM), while Sn 5p and I 5p orbitals in nonbonding state form conduction band minima (CBM). Despite having resemblance in ionic radii to Pb²⁺, the band energies of Sn orbitals are at a higher level and hence the position of CBM and VBM are higher in Sn-OIHPs. When interfaced with CTLs in either of the device configurations, the devices suffer from the poor band alignment and V_{oc} deficit (Fig. 4(a)). As the electrons shielding is weaker in Sn²⁺ as compared to Pb²⁺, it tends to easily lose 5s electrons and leads to oxidation. In addition, the band energy levels for Sn 5s are higher, which facilitates poor bond strength of Sn-X. Hence it easily reacts with the atmospheric oxygen. From a view point of the environmental stability, Bi or Sb WBG perovskites are promising alternatives. However, poor device performance in these cases can be attributed to intrinsic defect formation during film processing, which leads to promote trap density states and non-radiative recombinations.

4. Strategies to improve high efficiency Pb-free WBG PSC technology

To overcome the existing challenges as discussed above, the present section deals with the current progress toward PCE enhancement in Pb-free WBG PSCs including state-of-the art fabrication techniques adopted, strategies implemented for defect passivation, interfacial engineering, and stability enhancement (Fig. 4(b)).

4.1. Processing methods

4.1.1. Solution processing

Solvent engineering with one-step method.

During device fabrication, developing high quality perovskite is of great importance, which directly affect the overall device performance. The Pb-PSCs technology has been extremely progressed with precise fabrication techniques such as one-step, two-step methods, hot casting, vapor-assisted methods, and so on. Though the film fabrication processes are similar, Pb-free perovskites undergo the formation of poor-quality film. Due to high surface energies and high Lewis's acidity, the crystallization becomes faster, which leads to uncontrolled crystal growth, non-uniformity, and smaller grain size in the final film. This ultimately results in defect formation, penetration of moisture through excessive grain boundaries and restricts the device performance. To overcome these issues, some state-of-the-art fabrication methods were developed with below optimizations.

Solution processing for fabricating OIHPs is known to be easy in handling and a low-cost technique. To fabricate highly crystalline Pb-free WBG perovskite one needs to control the parameters for fabricating films such as solvent dripping time, annealing temperature, time, and etc. In one of the initial reports, DMF is used for MASnI_{3-x}Br_x perovskite precursor, where the perovskite films were deposited over TiO₂ layer in a planar structure to avoid the direct contact between transparent conducting oxide (TCO), hole transport layer (HTL) and metal contact [29]. However, the report suggested that Sn precursors suffer from poor solubility in DMF including fast crystallization. Zhang et al. [31] fabricated FASnI₂Br WBG (1.68 eV) perovskite for inverted device structure via one-step solution processing where 1 mL DMF was used to dissolve SnI₂ and FABr followed by spin coating of precursor solution at 2500 rpm with 20 μ L chlorobenzene dripping at 7 sec., which was annealed at 100–75 °C for 5 min, resulted in the formation of 200

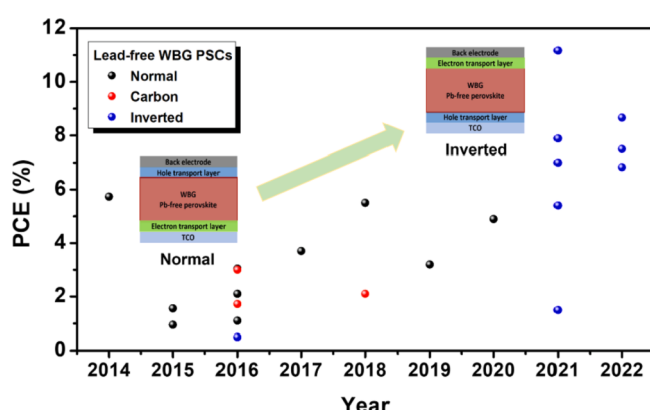


Fig. 3. Efficiency progress in Sn WBG PSCs in various device architectures.

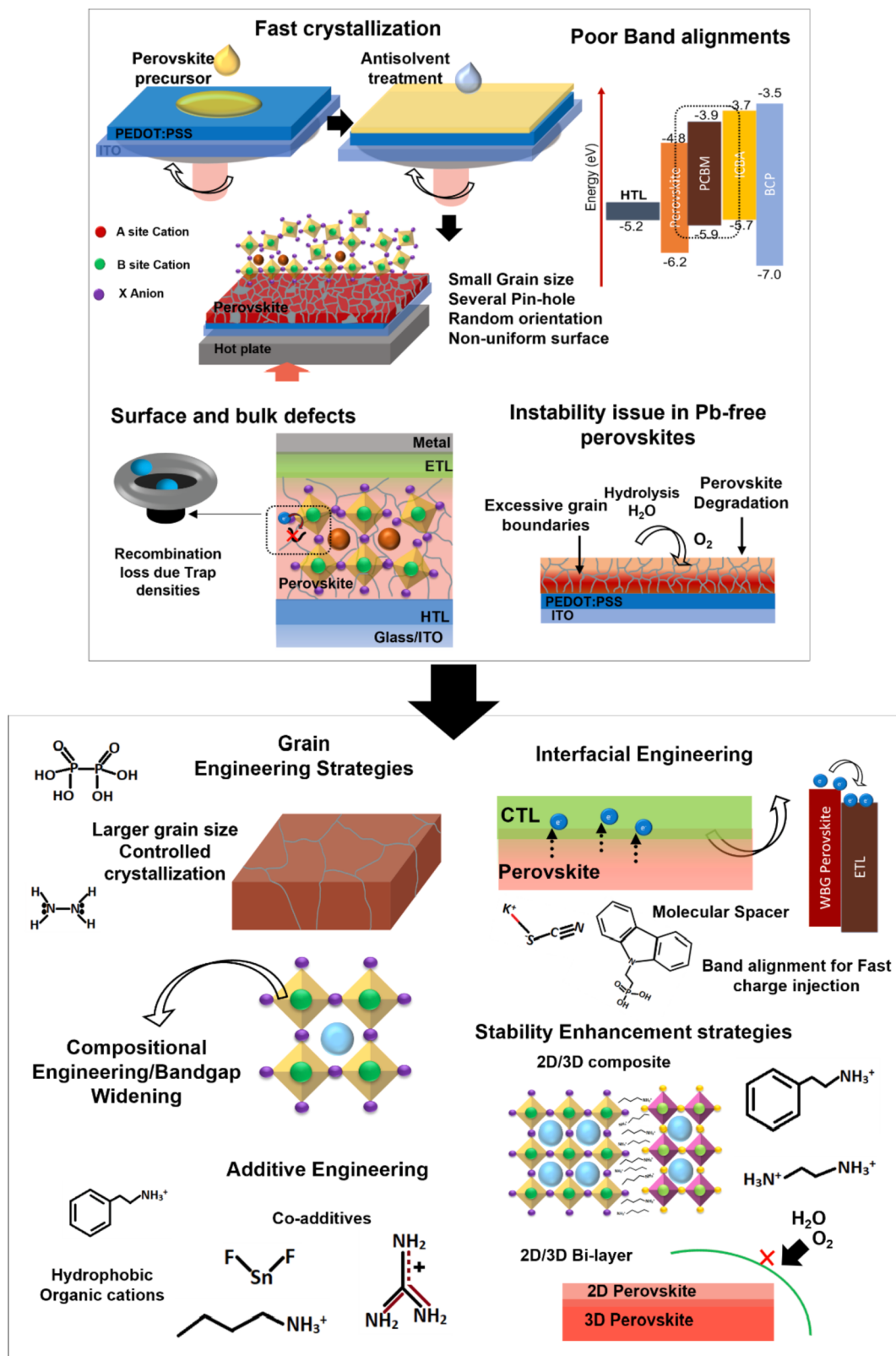


Fig. 4. (a) Illustrating issues associated with Pb-free WBG OIHPs i.e., fast crystallization tends to cause formation of smaller grain size with non-uniformity and random crystal orientation, associated surface and bulk defects, poor device interfaces, and band mismatch and instability. (b) Graphical representation of strategies to overcome these issues, such as processing techniques with grain engineering, compositional modifications and better alignments between the interfaces, trap density passivation, perovskite/CTL interface engineering, and stability enhancement.

nm thick perovskite film. The crystallization of Sn perovskite becomes uncontrolled and comparatively faster, hence annealing temperature and time both need to be optimized to get better film morphology. They examined the annealing of the fabricated film initially at 100 °C for 5 min resulted in the formation of worst film with patches and non-uniformity. To avoid these issues, the temperature and time were optimized to 75 °C for 5 min of annealing. As prolonged thermal treatment led to degradation of Sn perovskites, henceforth fabricating Sn WBG perovskite films via solution-processing needs to treat the optimal temperature of 70–75 °C for 5–10 min for complete crystallization.

Due to the solubility issues of SnX_2 precursors with DMF or GBL, reports revealed that DMSO can help in retarding the crystal growth rate by forming an intermediate adduct system i.e., $\text{SnX}_2\text{-3DMSO}$ results in controlled crystallization to a certain extent [34]. In addition, due to the high boiling point of DMSO (189 °C), evaporation during the annealing process becomes slower, which controls the crystal formation rate. Considering these facts, DMSO was used in combination with DMF to retard rapid crystallization (Fig. 5(a)). Solvent engineering strategy is beneficial to control these issues and resulted in the fabrication of high-quality perovskite film. However, excessively high boiling point solvent in the mixed solvent system may damage the whole perovskite film, as inappropriate annealing time and temperature results in degradation and traces of precursor solvent in the final film. Large grain size with uniformity and reduced pinholes was achieved and a device with PCE of 3.20% was observed for $\text{MASnI}_{3-x}\text{Br}_x$ ($x = 0.767$, $E_g = 1.75$ eV) [35]. Hence for fabricating Pb-free WBG perovskite film, the ratio of DMSO in the precursor solution needs to get critically optimized. Over time and further optimizations, the state-of-the-art Sn WBG perovskite film deposition technique has been established as depicted in Fig. 5(b). Whereby to fabricate perovskite layer on top of PEDOT:PSS (HTL) comprising of FABr, SnI_2 , and SnF_2 in DMF:DMSO (4:1) mixed solution

system, further spin-coated on HTL at 5000 rpm for 50 sec with chlorobenzene (non-polar solvent) dripped at 10 sec from the start of spin-coating step, forms $\text{SnX}_2\text{-DMSO}$ intermediate phase which helps in controlling crystal growth, followed by annealing at 70 °C for 10 mins for complete crystallization and removal of excess solvent from the final film [36,37].

G. Liang et al. reported one step solution processing of $\text{Cs}_3\text{Bi}_2\text{I}_10$ WBG ($E_g \sim 1.78$ eV) perovskites and the formation of dense morphology with the PCE of 1.03% without hysteresis [38]. Non-toxic methyl acetate solvent processed $\text{MA}_3\text{Bi}_2\text{I}_9$ delivered the PCE ~ 1.12% and 1.62% in the mesoporous device where spiro-OMeTAD and P3HT used as HTLs, respectively [39]. The poor film quality of Bi perovskites is one of the factors causing inferior device performance, and it is related to chemical stoichiometry and film processing techniques. D. B. Khadka et al. explored solvent-annealing based post-antisolvent treatment to fabricate compact Bi perovskite ($\text{Cs}_3\text{Bi}_2\text{I}_9$ and $\text{CsBi}_3\text{I}_{10}$) [40]. The schematic of the typical synthesis procedure is shown in Fig. 5(c), where CA, AS and AS + SA represents conventional annealing, antisolvent annealing, and solvent annealing post-antisolvent, respectively. For CA method, CsI and BiI_3 precursor solution of 0.5 M in DMF:DMSO (7:3 (v:v)) is used to spin-coat at 1500–3000 rpm (20 sec) and directly annealed for 60 min at 90–200 °C. For AS method, 150 μL chlorobenzene dripped at 20th sec after coating perovskite precursor and the film was further annealed at 120 °C for 60 min. In the case of AS + SA method, post-antisolvent treated perovskite film was kept for annealing in presence of 5 μL DMF and annealed at 120 °C for 60 min. It was observed that, film prepared with AS + SA method shows high crystallinity with compactness. Likewise, these fabrication procedures were implemented to develop Sb perovskites as well. It is very crucial to control the processing protocols in Bi and Sb perovskites to form a compact and homogeneous film. The solution processing method with antisolvent treatment differs

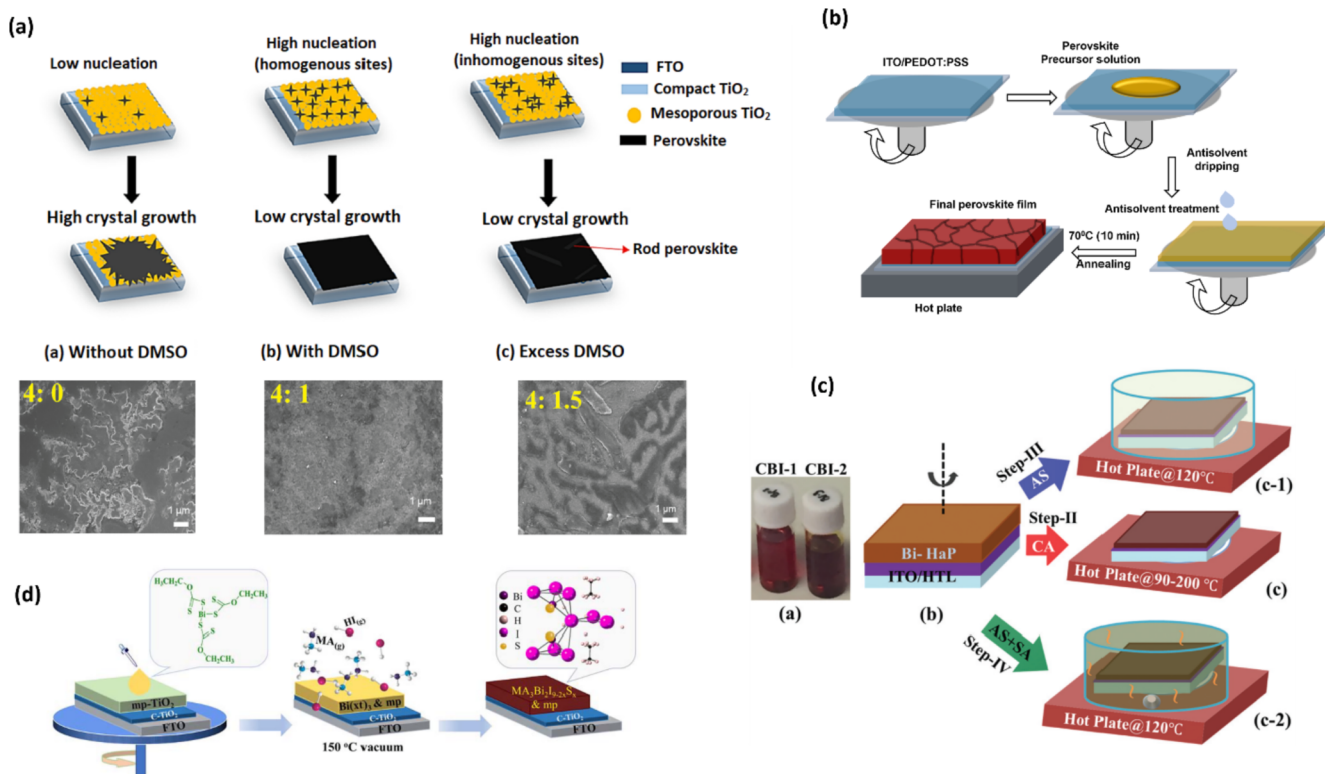


Fig. 5. (a) Graphical representation and SEM top-view of Sn perovskite film fabrication and effect of solvent engineering on the nucleation and growth process. Reproduced with permission from Elsevier. Copyright (2019) [35] (b) Illustration of one-step processing for Pb-free WBG perovskite fabrication. (c) Pictorial representation for fabricating Bi perovskite where c-1, c-2 and c-3 represent antisolvent annealing, conventional annealing, and solvent annealing post-antisolvent, respectively. Reproduced with permission from Royal society of chemistry. [40]. (d) Graphical illustration of low-pressure vapor assisted solution processing of Sb-incorporated Bi perovskite. Reproduced with permission from John Wiley and Sons. Copyright (2019) [49].

from CA for Sb WBG perovskite, where toluene with a small amount of SbI_3 dripped during antisolvent treatment to compensate iodine deficiency. However, a higher local supersaturation level of nucleation and growth leads to fast crystallization of perovskite during anti-solvent annealing, forms a non-uniform film with smaller grain size [41]. A reduced supersaturation annealing strategy can be useful to control the rate of solvent evaporation during the annealing process of $\text{Rb}_3\text{Sb}_2\text{I}_9$ [42].

Two step-method.

We speculate that Pb free WBG perovskites may reach high device efficiencies with further efforts. One needs to focus on both J_{sc} and V_{oc} enhancement, which directly relates to the quality of perovskite film. The handling process of Pb-free WBG perovskites is quite different, hence during fabrication following points should be considered. (1) Control perovskite nucleation and growth rate to reduce non-radiative recombinations: the rapid crystallization forms non-uniform film that leads to develop intrinsic defects. It is highly recommended to use Sn metal powder in perovskite solution at every initial step to avoid further oxidation of Sn precursors. Especially during the fabrication of Sn WBG perovskites, it is important to maintain glove box and spin coater temperature, as they may also affect the film processing. The one-step method is a simple technique which deposits perovskite precursor followed with antisolvent-assisted crystallization or direct annealing. However, this technique may not fit to fabricate large scale uniform films, since the antisolvent dripping time in one-step method is very critical to control the growth rate and demand highly skilled handling with reproducibility, which is a key to fabricate Pb-free WBG perovskites. Previous studies on Sn perovskite fabrication with two-step method revealed that the sequential deposition method is more competitive to gain superior device performance and highly reproducible. The two-step deposition technique avoids the severity to control over antisolvent dripping, control the morphology of individual layers in sequential processing of perovskite and organic molecule layer, which is suitable to develop large scale device [43,44]. (2) Control over perovskite precursor stoichiometry: For instance, Sn WBG perovskite can be formed by tuning mixed halide ratio and hence the precision in compositional engineering and perovskite precursor stoichiometry plays a critical role. The accuracy in iodine to bromine ratio needs to follow perfectly, as the addition of excess bromine content may enhance the V_{oc} but results in deprived J_{sc} .

Vapor-assisted solution process.

Solution processing methods for Pb-free WBG perovskite underwent several advances to create a state-of the art processing technique. Several strategies have been implemented such as Lewis's acid-base adduct formation, solvent engineering, and organic molecule addition to retard the crystal growth and produce films with low defect density. Even self-p doping during film fabrication in Sn perovskites leads to poor device efficiencies. Yokoyama et al. used low-temperature vapor assisted solution process (LT-VASP) to fabricate $\text{MASnI}_{3-x}\text{Br}_x$ WBG perovskite [45]. Surprisingly SnBr_2 film leads to the formation of MASnBr_3 and at elevated temperature of phase formation, MAI supplies only MA gas during perovskite formation and hence a more prominent difference in bandgaps was observed. Consequently, extra Sn^{2+} source was supposed to be the part of final perovskite films in LT-VASP, helps in regulating Sn vacancies, which suggested low self p-doping level. The performance of one-step assisted PSCs did not show any extraordinary device performance i.e., PCE $\sim 0.14\%$, whereas, LT-VASP based devices showed diode like behavior. This finding may help in determining how one can control self p-doping in Sn perovskites [45]. Jung et al. reported sequential-evaporation technique to deposit MASnBr_3 on top of TiO_2 , with reduced oxidation. Adopting this technique, the upper MABr layer helps in protecting the oxidation of perovskite when exposed to air. The obtained film showed high crystallinity and high optical absorption with PCE of 1.12% for WBG PSCs [46].

Vapor assisted solution method by subjecting BiI_3 film to MAI vapors push the PCE to 3.17% ($J_{sc} \sim 4.02 \text{ mA.cm}^{-2}$, $V_{oc} \sim 1.01 \text{ V}$ and FF \sim

0.78) for $\text{MA}_3\text{Bi}_2\text{I}_9$ ($E_g \sim 1.87 \text{ eV}$) WBG PSC [47]. S. M. Jain et al., exploited vapor assisted method to develop uniform and compact $\text{MA}_3\text{Bi}_2\text{I}_9$ perovskite film. In the typical procedure, the BiI_3 solution was spin-coated and kept under MAI vapors during annealing. Solid MAI at higher temperature dissociates into methylamine and hydrogen iodide gas that further reacts with BiI_3 to form $\text{MA}_3\text{Bi}_2\text{I}_9$. Compared to one-step solution processing which forms non-uniform Bi perovskite film [48], fabrication through VASP method is more successful as BiI_3 grains in the first step act as nucleation sites which later react with MAI vapors to develop homogeneous film with better surface coverage. With further modifications in VASP method, J. Li et al. fabricated $\text{MA}_3\text{Bi}_2\text{I}_{9.2x}\text{S}_x$ perovskite through the low pressure-VASP method [49]. As shown in Fig. 5(d), $\text{Bi}(\text{xt})_3$ ($\text{xt} = \text{ethyl xanthate}$) solution was spin-coated and film was kept in a covered petri plate under 10 kPa pressure at 150 °C. Here MAI powder was scattered uniformly. High temperature annealing is necessary to develop Sb perovskite, however straightforward annealing at more than 200 °C is not feasible, as it leads to the decomposition of perovskite. F. Li et al. explored a modified technique to reduce the chance of $\text{Rb}_3\text{Sb}_2\text{I}_9$ decomposition even at higher annealing temperature by keeping SbI_3 powder in the closed vicinity of as-spun film [42]. In this high temperature vapor annealing method of SbI_3 powder with a low melting point (170 °C) was kept under covered atmosphere with the as spun perovskite film at an elevated temperature of 225 °C, to compensate the loss of SbI_3 during annealing.

4.1.2. Sequential vacuum deposition

Sequential deposition of CsBr (58.5 nm)/ SnBr_2 (133 nm)/ CsBr (58.5 nm) under 10^{-6} torr followed by a solid-state reaction at 230 °C under nitrogen atmosphere for 60 min inside glove box resulted in the formation of thick perovskite film of 250 nm. To avoid the handling of solvents and associated degradations of perovskite film, Fang et al., reported sequential vacuum deposition of WBG CsSnBr_3 in a planar heterojunction device with PCE $\sim 1.5\%$ [50]. Such deposition procedure is beneficial to avoid solvent and air instability related issues for Sn WBG perovskites and may help in technological advancement in the future.

4.2. Compositional engineering

4.2.1. Cation substitution

Compositional engineering is an effective strategy to tune optoelectronic properties by modifying the E_g . It is interesting to understand the phenomenon behind E_g modulations via cation substitution, since VB and CB of OIHPs formed due to metal-halide interaction, where VBM is associated to metal s-halogen p antibonding orbital overlapping and CBM formed with metal p-halogen p orbital interaction in non-bonding states. Apart from this fact, A site cation counterbalance the whole structure, however the substitution with smaller ionic radii cation leads to a different phenomenon in Pb and Sn-based perovskites. In Pb halide perovskite large A site cation substitution with a smaller one leads to octahedral tilting, on the other hand in Sn perovskites large cation replacement with a smaller cation result in lattice contraction. Due to different phenomenon of octahedral-tilting and lattice contraction, the opposite trends in E_g modulation have been observed. In the former condition it results in E_g enhancement, although in the latter case E_g may shift towards the lower energies by substituting large A site cation with the smaller cations such as Cs^+ or MA^+ and so on [51]. In 3D Sn perovskites, the incorporation of ethylenediammonium cation "en" forms hollow perovskite without hampering the crystal dimensionality. The 3D hollow Sn perovskite was first introduced by kanatzidis group who figured out the concept of "hollow perovskite" based on formation of Schottky defects [52]. With non-periodicity reduction in molecular orbital overlapping between Sn-I atoms, it leads to the reduction in VB and CB widths, and increases the E_g from 1.4 to 1.9 eV [52]. Tsai et al., [53] synthesized $\text{HEA}_x\text{FA}_{1-x}\text{SnI}_3$ with E_g modulation from 1.34 eV ($x = 0$) to 2.07 eV ($x = 1$) and a significant shifting in VBM from -4.91 eV ($x = 0$) to -5.50 eV ($x = 1$) was observed (Fig. 6(a)). Here $\text{HEA}_{0.6}\text{FA}_{0.4}\text{SnI}_3$

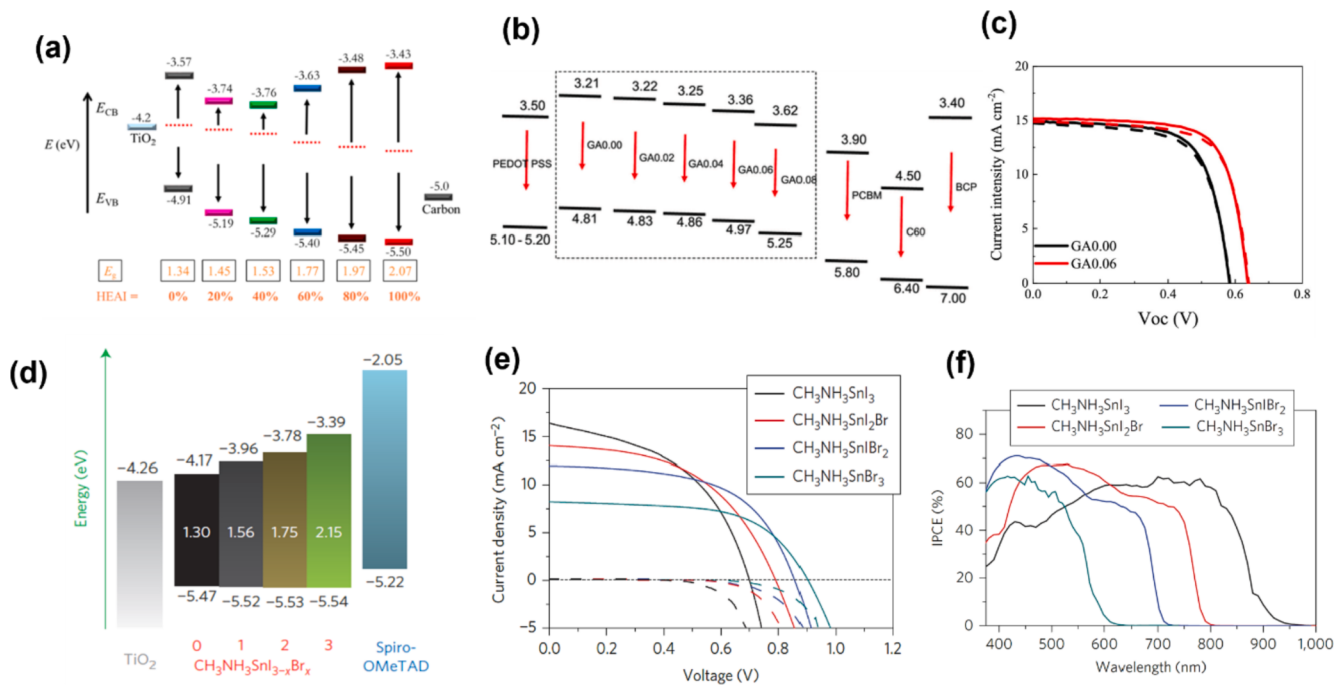


Fig. 6. (a) Energy band diagram for $\text{HEAxFA}_{1-x}\text{SnI}_3$ in carbon PSC architecture with illustrating the effect of cation doping on CB and VB shift. [53]. (b-c) Energy band alignments of $\text{GA}_x(\text{FA}_{0.8}\text{Cs}_{0.2})_{1-x}\text{SnI}_2\text{Br}$ in p-i-n PSC and corresponding J-V characteristics. Reproduced with permission from American Chemical Society. Copyright (2021) [54]. (d-f) Energy band diagram of $\text{MASnI}_{3-x}\text{Br}_x$ n-i-p PSC. J-V characteristics and IPCE graphs for $\text{CH}_3\text{NH}_3\text{SnI}_{3-x}\text{Br}_x$ PSCs ($x = 0, 1, 2, 3$). Reproduced with permission from Springer Nature. Copyright (2014) [29].

and $\text{HEA}_{0.8}\text{FA}_{0.2}\text{SnI}_3$ PSC displayed the PCE of 2.1% ($J_{sc} \sim 10.68 \text{ mA cm}^{-2}$ and $V_{oc} \sim 0.38 \text{ V}$) and 1.3% ($J_{sc} \sim 6.61 \text{ mA cm}^{-2}$ and $V_{oc} \sim 0.40 \text{ V}$), respectively. Song et al. reported the PCE of 5.4% for $\text{GA}_{0.2}\text{FA}_{0.8}\text{SnI}_3:\text{EDAI}_2(15\%)$ WBG ($E_g = 1.61 \text{ eV}$) [30]. It was found that gradual addition of EDAl₂ in $\text{GA}_{0.2}\text{FA}_{0.8}\text{SnI}_3$ widen E_g from 1.39 to 1.61 eV for 15% EDAl₂ added perovskite, and further increased to 1.65 eV with 20% EDAl₂ addition. Hayase group explored Sn WBG perovskite by incorporating formamidinium (FA^+) and guanidinium (GA^+) in CsSnI_2Br and reported a respectable PCE of 7.0% for $\text{GA}_{0.06}(\text{FA}_{0.8}\text{Cs}_{0.2})_{0.94}\text{SnI}_2\text{Br}$ [54]. The investigation revealed a significant E_g widening from 1.41 to 1.68 eV with increasing FA^+ ratio in $\text{FA}_x\text{Cs}_{1-x}\text{SnI}_2\text{Br}$ and the best PCE of 4.80% was achieved for

$\text{FA}_{0.8}\text{Cs}_{0.2}\text{SnI}_2\text{Br}$ ($E_g \sim 1.6 \text{ eV}$) as compared to CsSnI_2Br device (PCE $\sim 1.68\%$). Furthermore, the incorporation of GA^+ in triple-cation perovskites helps in modulating the CB and VB, developing proper alignment with transport layers. The PCE of 5.93% was reported for fresh device of $\text{GA}_{0.06}(\text{FA}_{0.8}\text{Cs}_{0.2})_{0.94}\text{SnI}_2\text{Br}$, while aging the device showed impressive PCE $\sim 7.0\%$ (Fig. 6(b-c)) [54], due to the reduced carrier recombination between perovskite and HTL.

Experimentally, Ge perovskites exhibit a direct bandgap in the range of 1.6–2.5 eV. In past few years, limited research groups utilized Ge in PSCs, where very poor device performance of 0.11% and 0.2% was reported for CsGeI_3 ($E_g \sim 1.63 \text{ eV}$) and MAGEI_3 ($E_g \sim 2.0 \text{ eV}$) PSCs [55]. In another approach for enhancing the PCE of MAGEI_3 , Br^- incorporation

Table 1
Photovoltaic parameters for cation and halide substituted WBG PSCs.

Material	Bandgap E_g (eV)	Device structure	J_{sc} (mA cm^{-2})	V_{oc} (V)	FF	PCE (%)	Ref.
Cation substitution							
$\text{HEA}_{0.6}\text{FA}_{0.4}\text{SnI}_3$	1.77	Carbon PSC	10.68	0.38	0.49	2.1	[53]
$\text{HEA}_{0.8}\text{FA}_{0.2}\text{SnI}_3$	1.97		6.61	0.40	0.47	1.3	
$\text{GA}_{0.2}\text{FA}_{0.8}\text{SnI}_3$ SnF ₂ (20%) EDAl ₂ (15%)	1.61	FTO/TiO ₂ /perovskite/Al ₂ O ₃ /ITO	17.8	0.51	0.58	5.4	[30]
$\text{GA}_{0.06}(\text{FA}_{0.8}\text{Cs}_{0.2})_{0.94}\text{SnI}_2\text{Br}$	1.60	FTO/PEDOT:PSS/perovskite/PC ₆₁ BM/C ₆₀ /BCP/Ag	15.16	0.64	0.72	7.00	[54]
$\text{Cs}_{1.99}\text{Li}_{0.01}\text{AgBiBr}_6$	1.82	FTO/TiO ₂ /perovskite/carbon	3.15	1.17	0.69	2.57	[57]
$\text{Cs}_2\text{AgBiBr}_6$ (PEA + 6%)	2.27	ITO/PEDOT:PSS/Cs ₂ AgBiBr ₆ /PCBM/BCP/Al	2.76	1.06	0.61	1.78	[58]
$\text{Rb}_{0.15}\text{Cs}_{2.85}\text{Sb}_2\text{Cl}_{19-x}$	2.07	FTO/Nb ₂ O ₅ /Pero/P3HT/carbon	4.91	0.88	0.57	2.46	[59]
Halide substitution							
$\text{CsSnI}_2\text{Br}_2$	1.65	FTO/TiO ₂ /perovskite/spiro-OMeTAD/Au	11.57	0.31	0.43	1.56	[60]
CsSnBr_3	1.75		3.99	0.41	0.58	0.95	
$\text{Cs}_2\text{SnI}_2\text{Br}_4$	1.63	FTO/TiO ₂ /Pero HTM/LPAH/FTO	3.41	0.57	0.54	1.08	[61]
MASnIBr_2	1.75	FTO/TiO ₂ /perovskite/Spiro-OMeTAD/Au	12.30	0.82	0.57	5.73	[34]
MASnBr_3	2.15		8.26	0.88	0.59	4.27	
FASnI_3 (Br ~25mol%)	1.63	FTO/bl-TiO ₂ /mp-TiO ₂ /perovskite/Spiro-OMeTAD/Au	19.8	0.41	0.66	5.5	[62]
$\text{MASnBr}_{1.8}\text{Cl}_{0.2}$	1.97	FTO/TiO ₂ /Al ₂ O ₃ /perovskite/Carbon	13.99	0.38	0.57	3.11	[63]
$\text{Cs}_2\text{Bi}_{2.6}\text{Br}_3$	1.74	ITO/NiO _x /Cs ₃ Bi ₂ 9-xBr _x /PC ₆₁ BM/C ₆₀ /BCP/Ag	3.15	0.64	0.57	1.15	[65]
$\text{Cs}_2\text{AgBiBr}_{5.8}\text{S}_{0.1}$	2.32	Electrode/HTM/Cs ₂ AgBiBr _{6-2x} S _x /m-TiO ₂ /c-TiO ₂ /FTO	3.2	0.93	0.65	1.9	[66]
$\text{Cs}_3\text{Sb}_2\text{I}_{9-x}\text{Cl}_x$ ($x = 0.71$)	2.21	ITO/PEDOT:PSS/perovskite/PC ₆₀ BM/Al	6.39	0.72	0.47	2.2	[67]

slightly increased the PCE $\sim 0.68\%$ for $\text{MAGeI}_{2.7}\text{Br}_{0.3}$ ($E_g \sim 2.1$ eV) [56]. Poor J_{sc} in Bi double PSCs is one of the serious issues, which severely affects the device performance. It has been observed that 'A' site doping with Li^+ and Rb^+ in double-perovskites controls the grain growth, reduces defects, and helps in PCE enhancement by increasing the J_{sc} to $3.15 \text{ mA}\cdot\text{cm}^{-2}$ for $\text{Cs}_{1.99}\text{Li}_{0.01}\text{AgBiBr}_6$ (Table 1) as compared to the controlled $\text{Cs}_2\text{AgBiBr}_6$ ($J_{sc} \sim 2.43 \text{ mA}\cdot\text{cm}^{-2}$) PSCs [57]. PEABr addition in perovskite precursor also helps in improving device performance, intrinsic defects and self-trapped exciton reduction was observed by the addition of PEA^+ cation which brings cation ordering and improved charge conduction [58,59]. Furthermore, substitution of Rb^+ at A site suppress the formation of 0D phase and passivate surface defects, which contributed attaining the best PCE of 2.46% ($V_{oc} \sim 0.88$ V) for $\text{Rb}_{0.15}\text{Cs}_{2.85}\text{Sb}_2\text{Cl}_x\text{I}_{9-x}$.

4.2.2. Halide substitution

Halide substitution brings ambient stability as well as enhancement of the E_g for desired WBG PSCs. Mhaisalkar group investigated in detail the E_g broadening in CsSnI_3 by Br^- incorporation [60]. The E_g transition observed from 1.27 eV (CsSnI_3) to 1.37 eV (CsSnI_2Br), 1.65 eV (CsSnIBr_2) and 1.75 eV (CsSnBr_3). The variation in film color was also observed from black-brown and then light brown, which affects the PSC performance. The PCE of 1.66% achieved for CsSnI_3 with low $V_{oc} \sim 0.20$ V, however with increasing Br^- concentration, reduction in J_{sc} was observed from 22.72 to $15.06 \text{ mA}\cdot\text{cm}^{-2}$ (CsSnI_2Br), which was further reduced to $11.57 \text{ mA}\cdot\text{cm}^{-2}$ (CsSnIBr_2) and $3.99 \text{ mA}\cdot\text{cm}^{-2}$ (CsSnBr_3). The E_g enhancement with Br^- incorporation and reduction in background carrier-densities, suppressed the charge recombination and increased V_{oc} from 0.20 V (CsSnI_3) to 0.41 V (CsSnBr_3). Lee et al., fabricated $\text{Cs}_2\text{SnI}_{6-x}\text{Br}_x$ mixed anion perovskite by electro-spraying deposition with E_g tuning. With formation of CsI clusters and dendrites, better-quality film was found. A prominent E_g modulation was observed for I^- to Br^- incorporation ($E_g \sim 1.30\text{--}2.85$ eV) and PCE of 1.08% was achieved for $\text{Cs}_2\text{SnI}_2\text{Br}_4$ WBG PSC [61].

Similarly, E_g adjustment in MASnI_3 can also be achieved by partial or complete replacement of I^- with Br^- , result in gradual broadening of E_g ($1.30\text{--}2.15$ eV) [34]. In a very first report on $\text{MASnI}_{3-x}\text{Br}_x$ WBG PSCs, the respectable PCE of 4.27% was reported for MASnBr_3 ($E_g \sim 2.15$ eV). Schematic representation of band alignment of $\text{MASnI}_{3-x}\text{Br}_x$ with TiO_2 and spiro-OMeTAD shown in Fig. 6(d) [29]. CB shifted from -4.17 eV (MASnI_3) to -3.78 eV (MASnIBr_2) and -3.39 eV (MASnBr_3), where E_g broadening caused due to CB shifting towards higher energies while VB remains unchanged. With increased Br^- ratio, J_{sc} reduced from $16.30 \text{ mA}\cdot\text{cm}^{-2}$ (MASnI_3) to $12.30 \text{ mA}\cdot\text{cm}^{-2}$ (MASnIBr_2) and $8.26 \text{ mA}\cdot\text{cm}^{-2}$ (MASnBr_3), however V_{oc} followed opposite trend, increased from 0.68 V (MASnI_3) to 0.82 V (MASnIBr_2) and 0.88 V (MASnBr_3) (Fig. 6(e)). The V_{oc} enhancement with increasing Br^- ratio may be ascribed to CB upshifting, whereas reduction in J_{sc} value is directly related to blueshift of absorption onset shown in IPCE spectra (Fig. 6(f)). The addition of Br^- in FASnI_3 uplifted the CB edge and eased the way for electron transport. The best PCE of 5.5% for 25 mol% Br doped FASnI_3 ($E_g \sim 1.63$ eV) was demonstrated [62].

Tsai et al. investigated the effect of varying $\text{SnBr}_2/\text{SnCl}_2$ concentration on device performance by mixing various ratios of $\text{SnBr}_2/\text{SnCl}_2$ with MAI precursor [63]. In the absence of SnCl_2 , the E_g was 1.81 eV, which further increased to 1.97 eV with the addition of SnCl_2 . The PCE of 3.11% observed for $\text{MASnIBr}_{1.8}\text{Cl}_{0.2}$. However, with increasing Cl^- ratio for $\text{MASnIBr}_{1.5}\text{Cl}_{0.5}$, the PCE reduced to 1.87% indicating that only small ratio of Cl^- in Sn WBG perovskites contributes in reducing carrier recombination. Photovoltaic parameters for compositional engineering in Pb-free WBG PSCs summarized in Table 1. Incorporation of PEAI or Sn (SCN)₂ in CsSnI_2Br leads to E_g widening from 1.59 eV (CsSnI_2Br) to 1.64 eV ($\text{CsSnI}_2\text{Br-PEA}$) and the reduction to 1.48 eV was observed for $\text{CsSnI}_{2-x}\text{Br}(\text{SCN})_x$ and $\text{CsSnI}_{2-x}\text{Br}(\text{SCN})_x\text{-PEA}$ perovskite. However, very poor PCE of 0.71% was realized for $\text{CsSnI}_2\text{Br-PEA}$ WBG PSC [64].

Halide mixing in Bi perovskites modulates E_g from 1.84 eV ($\text{Cs}_3\text{Bi}_2\text{I}_9$)

to 1.74 eV ($\text{Cs}_3\text{Bi}_2\text{I}_6\text{Br}_3$), which tends to increase PCE to 1.15% [65]. The substitution at X site by sulfur in double-perovskites leads to E_g tuning from 2.37 eV ($x = 0$) to 2.30 eV ($x = 0.15$) in $\text{Cs}_2\text{AgBiBr}_{6-2x}\text{S}_x$ and slight upshifting of VB edge was observed from -5.56 eV ($x = 0$) to -5.48 eV ($x = 0.15$) [66]. Unlike halide exchange of I^- to Br^- in Sb perovskite, the strategy of exchanging I^- with Cl^- improves the electronic properties, which contributes in passivating the deep defects and improving grain size. It was observed that the device PCE increased from 1.4% ($\text{Cs}_3\text{Sb}_2\text{I}_9$) to 2.2% [$\text{Cs}_3\text{Sb}_2\text{I}_{9-x}\text{Cl}_x$ ($x = 0.71$)] in the WBG layered PSC [67].

4.3. Additive engineering

The rapid crystallization issue in Pb-free WBG perovskite severely affect perovskite properties, resulted in the formation of surface and bulk defects. In addition, Sn perovskites suffer from instability when exposed to ambient atmosphere. This unavoidable issue leads to self p-type doping, which confines carrier diffusion length. SnF_2 additive acts as a reducing agent for Sn perovskite and has been using to upsurge the formation energy of Sn vacancy to mitigate self p-doping. It can reduce background carrier densities by neutralizing defect states. The PCE of 2.1% was observed for CsSnBr_3 ($E_g \sim 1.75$ eV) WBG PSC [28]. The investigation further revealed that SnF_2 as an additive assist in decreasing the ionization potential and work function of CsSnBr_3 so that it can match well with the HOMO level of HTL in PSCs. Xiao et al. investigated the addition of SnF_2 in perovskite precursor solution that plays a critical role in facilitating the formation of heterogeneous nucleation sites and enabling uniform crystal growth (Fig. 7(a)) [68]. They examined various ratios of SnF_2 and its effect on the morphology as shown in SEM micrographs (Fig. 7(b)). The film without SnF_2 showed non-uniform surface coverage which improved by adding SnF_2 . At the optimized SnF_2 of 30% , complete coverage with uniformity was observed in the perovskite film with the PCE $\sim 3.70\%$ ($J_{sc} \sim 13.77 \text{ mA}\cdot\text{cm}^{-2}$, $V_{oc} \sim 0.45$ V and FF ~ 0.59) for MASnIBr_2 ($E_g \sim 1.70$ eV) WBG PSC. Additional investigations suggest that 20 mol% SnF_2 in CsSnBr_3 WBG perovskite reduces the oxidation rate of Sn^{2+} , and suppresses the formation of multiple phases. Furthermore, it promotes the rearrangement of Sn 5 s orbitals, resulted in VBM shift more towards fermi level [69]. SnF_2 doping certainly reduces defect densities in Sn WBG perovskites as investigated by Zhang et al. Time resolved PL observation showed prolonged bimolecular-lifetime component for SnF_2 doped FASnI_2Br and the PCE of 10% SnF_2 -doped FASnI_2Br realized 7.6% in p-i-n configuration [70]. Li et al. explored the addition of small amount of hypophosphorous acid (HPA) as a co-additive in CsSnIBr_2 precursor solution to increase the nucleation rate and control further oxidation [71]. The PCE was improved to 3.0% with enhanced stability at higher temperature as compared to the controlled device PCE $\sim 1.7\%$. Kanatzidis group introduced hydrazine vapor as strong reducing agent before spin-coating, which improved film quality (Fig. 7(c)) [72]. Through the plausible reaction $2\text{SnI}_6^{2-} + \text{N}_2\text{H}_4 \rightarrow 2\text{SnI}_4^{2-} + \text{N}_2 + 4\text{HI}$, Sn^{2+} vacancies get suppressed in CsSnBr_3 ($E_g \sim 1.80$ eV) with longer lifetime of 3.01 ns, which indicates reduced trap densities and defect passivation. Therefore, the device PCE of 3.04% was achieved.

Previous studies suggest that hydrophobic organic cations e.g., EDAI_2 , BAI or PHSCN can effectively suppress the trap densities [43,73]. Chen et al. investigated that the optoelectronic properties of $\text{GA}_{0.06}(\text{FA}_{0.8}\text{Cs}_{0.2})_{0.94}\text{SnI}_2\text{Br}$ WBG ($E_g \sim 1.62$ eV) perovskite can be improved by exploring GeI_2 and EDABr_2 addition [74]. Furthermore, they observed PCE enhancement to 7.50% ($V_{oc} \sim 0.60$ V) for ethylenediamine passivated $\text{EDA}_{0.01}(\text{GA}_{0.06}(\text{FA}_{0.8}\text{Cs}_{0.2})_{0.94})_{0.98}\text{SnI}_2\text{Br}$ PSC. The excess organic additives help in regulating crystal growth in halide perovskites. H. Wu et al. used MABr volatile additive to control crystallization process in $\text{Cs}_2\text{AgBiBr}_6$ double perovskite, achieved PCE of 2.53% ($V_{oc} \sim 0.99$ V and $J_{sc} \sim 3.07 \text{ mA}\cdot\text{cm}^{-2}$) [75]. MABr additive can control the perovskite crystallization and improves film morphology (Fig. 7(d)). To control the crystallinity and film uniformity in $\text{MA}_3\text{Sb}_2\text{I}_9$ ($E_g \sim 1.95$ eV) and $\text{Cs}_3\text{Sb}_2\text{I}_9$ ($E_g \sim 2.0$ eV), hydroiodic acid (HI) as an

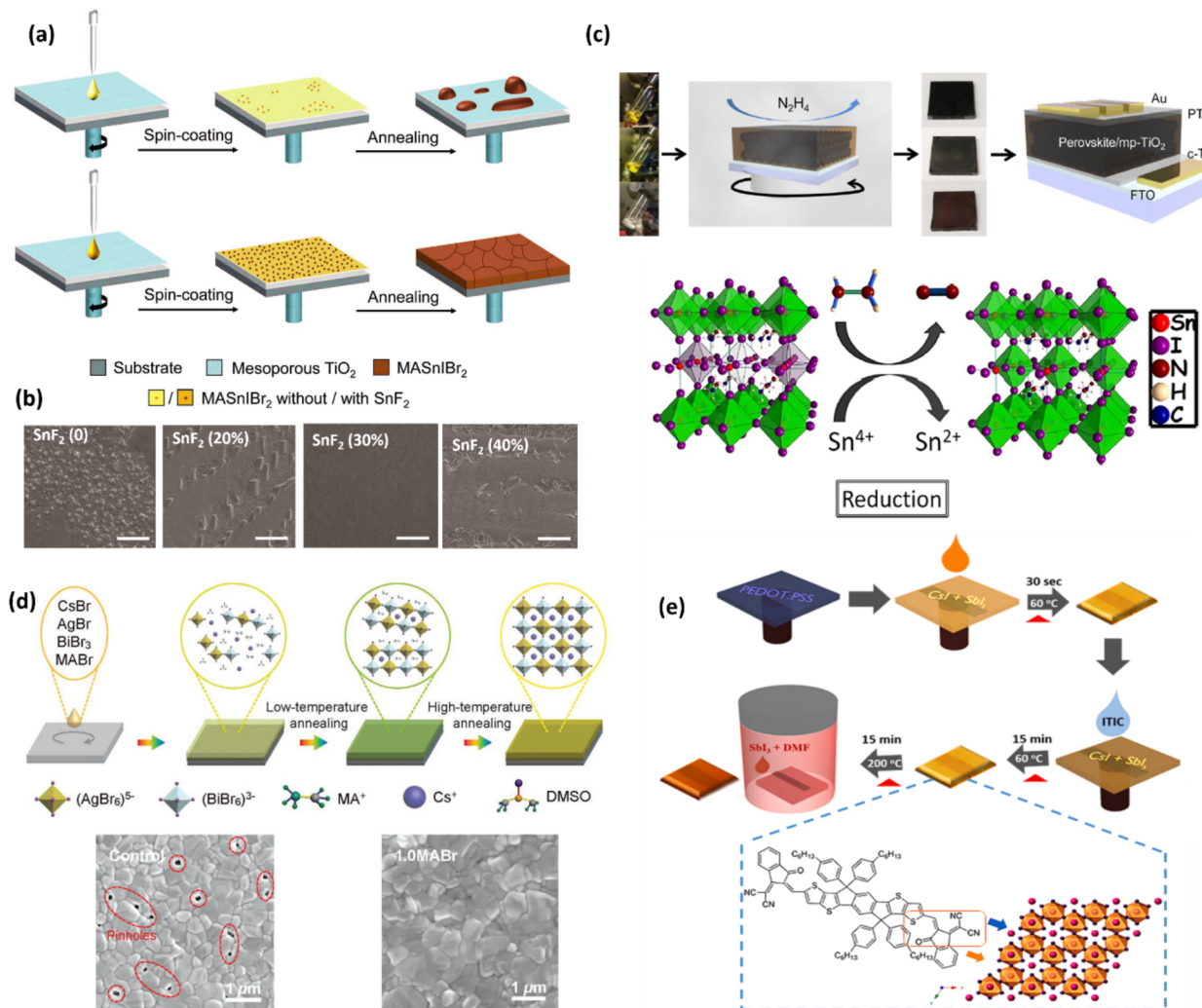


Fig. 7. (a) Schematics of nucleation and growth procedure of Sn WBG perovskite without and with SnF_2 additive, (b) SEM micrograph (3 μm scale) of as fabricated perovskite films with different concentrations of SnF_2 additive i.e., without SnF_2 (0%), with SnF_2 20%, 30% and 40%. Reproduced with permission from John Wiley and Sons. Copyright (2017) (c) Top: Schematic representation for fabricating MASnI_3 , CsSnI_3 and CsSnBr_3 (top to bottom in image) films in reduced vapor atmosphere and related device architecture. Bottom: Plausible mechanism to depict the reaction between hydrazine and Sn perovskites (d) Graphical representation of double perovskite processing with MABr as additive and SEM micrographs for controlled and MABr additive assisted $\text{Cs}_2\text{AgBiBr}_6$ double perovskite [75] Reproduced with permission from John Wiley and Sons. Copyright (2021) (e) Pictorial representation of fabricating $\text{Cs}_3\text{Sb}_2\text{I}_9$ with ITIC. Reproduced with permission from Elsevier. Copyright (2021) [81].

additive in perovskite precursor assists in reducing porosity and further improving film morphology [76]. F. Umar et al. employed hydrochloric acid (HCl) as intermediate additive in perovskite precursor [77]. It has been observed that the HCl coordinates with $\text{Cs}_3\text{Sb}_2\text{I}_9$ to control the film morphology. P. Karuppuswamy et al. employed chlorobenzene anti-solvent treatment and introduced perylene/pyrene hydrophobic scaffold in $(\text{MA})_3\text{Sb}_2\text{I}_9$ during film fabrication process to speed up heterogeneous nucleation in order to achieve perovskite film with large grain size [78]. With improved film morphology, $\text{MA}_3\text{Sb}_2\text{I}_9$ PSC delivered the PCE of 2.77% ($V_{\text{oc}} \sim 0.70$ V and $J_{\text{sc}} \sim 6.64 \text{ mA}\cdot\text{cm}^{-2}$). It has been further investigated that the crystallization rate can be regulated by using Lewis's base adducts strategy in D- $\text{Cs}_3\text{Sb}_2\text{I}_9$. Thiourea (S-donor) and NMP O-donor Lewis's base helps in retarding crystal growth and developing good morphology of perovskite film [79,80]. Indacenodithiophene (ITIC) with C = O and C≡N functional groups forms Lewis's acid-base adduct with Cs^+ and Sb^{3+} during pre-annealing at 60 °C, that retards perovskite crystallization (as shown in Fig. 7(e)) and contributes to improve film morphology. It also acts as CTL to facilitate better charge extraction and thus the PCE ~ 3.25% ($V_{\text{oc}} \sim 0.91$ V and $J_{\text{sc}} \sim 6.45 \text{ mA}\cdot\text{cm}^{-2}$) was achieved in $\text{Cs}_3\text{Sb}_2\text{I}_9$ /ITIC heterostructure based PSC

[81]. Nazeeruddin group demonstrated that introducing Li-TFSI in $\text{MA}_3\text{Sb}_2\text{I}_{9-x}\text{Cl}_x$ leads to the formation of intermediate phase of 0D MAI-SbCl₃-Li-TFSI which slower down the dimensional transformation to 2D structure and stabilize E_g to 2.0 eV [82]. The best PCE of 3.34% ($V_{\text{oc}} \sim 0.70$ V and $J_{\text{sc}} \sim 7.38 \text{ mA}\cdot\text{cm}^{-2}$) was reported, which retained up to 90% after 1400 h in ambient atmosphere.

4.4. Interfacial modifications

With multiple advancement through compositions and defect passivation, Pb-free WBG PSCs successfully reached to respectable PCEs. However, to implement such device technology in TSCs as potential WBG front sub-cells, it is crucial to overcome V_{oc} deficit issue. A recent report investigated the role of interfacial modification at perovskite/HTL interface by introducing 2PACz as monolayer (approx. 1 nm). The conductivity and charge carrier concentration improved in PEDOT:PSS/2PACz bilayer HTL, where the existence of S^+ in PEDOT contributed to conductivity enhancement (Fig. 8(a)). The concepts of bilayer can also help in reducing the valence band offsets down to -5.73 eV for PEDOT:PSS/2PACz as compared to PEDOT:PSS (-5.10 eV), which affects V_{oc}

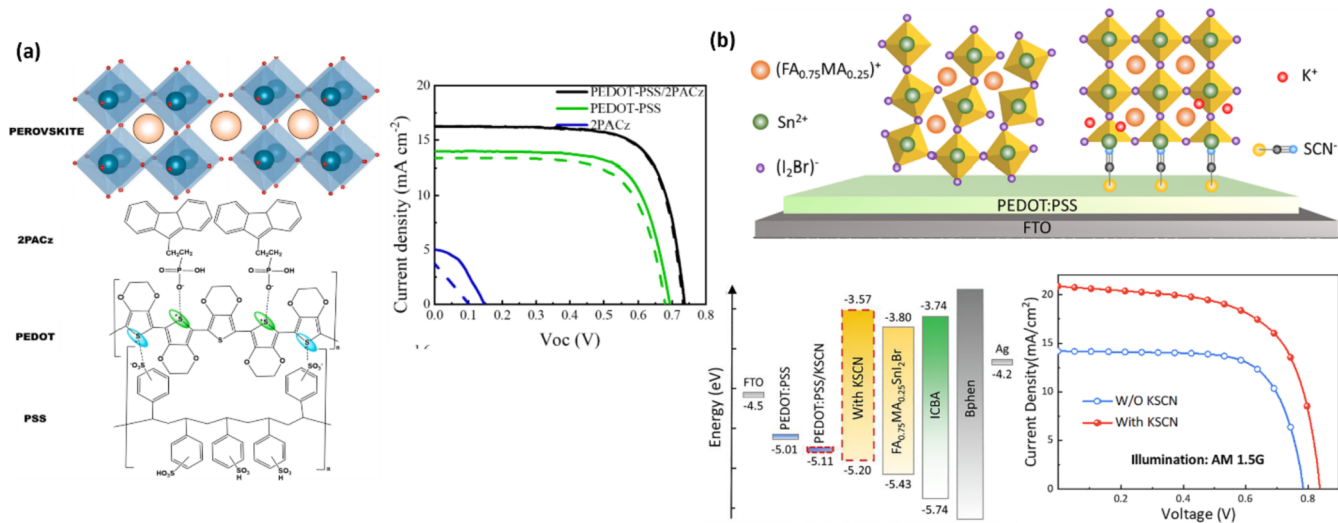


Fig. 8. (a) Structural representation of PEDOT:PSS/2PACz/perovskite and relative J-V characteristics for Sn WBG PSC [37] (b) Schematics shows preferential orientation of FA_{0.75}MA_{0.25}SnI₂Br perovskite with KSCN, band energy alignments of perovskite with respect to HTL/ETL in p-i-n architecture, J-V characteristic comparison for without and with KSCN treated perovskites with 11.17% PCE. Reproduced with permission from Elsevier. Copyright (2022) [32].

enhancement from 0.69 V to 0.74 V for the champion device [37]. In another recent report, Cao et al. demonstrated the bottom surface passivation approach by introducing potassium thiocyanate (KSCN) in FA_{0.75}MA_{0.25}SnI₂Br ($E_g \sim 1.63$ eV) perovskite (Fig. 8(b)) [32]. The fabricated device on p-i-n architecture, where ICBA used as electron transport layer (ETL) showed better band energy match with perovskite/KSCN. With multiple engineering strategies V_{oc} for the champion device reached to 0.82 V with the PCE of 11.17% for FA_{0.75}MA_{0.25}SnI₂Br WBG PSC.

Bi and Sb WBG perovskites suffer from poor charge extraction and deprived J_{sc} . X. Yang et al. realized J_{sc} enhancement from 4.49 mA·cm⁻² to 5.31 mA·cm⁻² in Cs₂AgBiBr₆ PSCs by introducing N719 dye between Cs₂AgBiBr₆/Spiro-OMeTAD interface [83]. The N719 dye molecule assisting suitable band alignments between perovskite and Spiro-OMeTAD accelerates charge extraction, and sunlight absorption capacity was also enhanced, which collectively increased the PCE to 2.84%. Another study demonstrated that J_{sc} can be improved by applying MoO₃ as energy gradient between P3HT/PTAA in Cs₂AgBiBr₆ n-i-p device [84]. To resolve the issue of poor J_{sc} , B. Wang et al. introduced Zn-Chlorophyll photoactive HTL, which showed J_{sc} improvement from 3.02 mA·cm⁻² (ITO/SnO₂/Cs₂AgBiBr₆/Spiro-OMeTAD/Ag) to 3.83 mA·cm⁻² (PCE ~ 2.79%) for ITO/SnO₂/Cs₂AgBiBr₆/Zn-Chl/Ag [85]. One of the recent studies reported highest $V_{oc} \sim 1.18$ V in planar Cs₂AgBiBr₆ PSC by incorporating PEABr in perovskite precursor solution and realizing the formation of 2D/3D double perovskite with maximum PCE boosted up to 2.5% [86]. The enhancement in V_{oc} is attributed to better energy level matching that leads to improved hole extraction.

Typically, Sb WBG PSCs suffer from poor V_{oc} and to enhance both J_{sc} and V_{oc} in Cs₃Sb₂I₉ PSC A. Hiltunen et al. replaced conventional Spiro-OMeTAD (HTL) with P3HT in planar device [87]. The VBM of Cs₃Sb₂I₉ and P3HT lies at -5.16 eV and -5.0 eV respectively. P3HT with better band alignment with perovskite may reduce the issue of V_{oc} deficit. A record PCE of 3.57% ($V_{oc} \sim 0.78$ V and $J_{sc} \sim 7.65$ mA·cm⁻²) was achieved for bulk heterojunction of 0.5Cs₃Sb₂I₉-Ag₃Bi₂I₉ PSC, executed by controlled crystal growth and better band-alignments that resulted in efficient charge carrier transport [88]. Charge extraction using transition metal dichalcogenides (TMD) at perovskite/ETL interface can be also used as an effective strategy to improve device performance. The PCE of 3.42% ($J_{sc} \sim 7.37$ mA·cm⁻²) was attained for PEDOT:PSS/Cs₃Sb₂Cl_xI_{9-x}/PMMA/TMD(WS₂)/PCBM as compared to the controlled device (PCE ~ 2.85% and $J_{sc} \sim 6.55$ mA·cm⁻²) without TMD [89].

4.5. Stability enhancement strategies

Another major challenge here is related to the poor stability of Sn WBG perovskite films which restrict the operational conditions and is considered as a serious issue that needs to be resolved urgently to develop Pb-free PSCs technology. As discussed earlier fast crystallization leads to uncontrolled and non-uniform perovskite morphology. That associates with the formation of excessive grain boundaries which is one of the ways for moisture penetration and hence degrades the perovskite film in seconds. In addition, more active s electrons in Sn perovskites ease further oxidation of Sn²⁺ to Sn⁴⁺ state which is unavoidable. Considering these facts enormous efforts have been made till date for stability enhancement by opting several strategies. Such as grain engineering strategies directly control the nucleation and growth of perovskites only to a certain extent, which includes solvent engineering and annealing temperature optimizations as discussed earlier. Even additives and compositional engineering strategies play a critical role in controlling the grain formation and reducing the oxidation of Sn perovskite.

In this line Liu et al. fabricated CsSn_{0.6}Ge_{0.4}I₃ (Eg greater than 1.62 eV) nanocrystal (NCs) PSC [90]. The stability of both perovskite NCs was investigated in detail using XPS after 10 min exposure to air (Fig. 9(a)). In only CsSnI₃, Sn⁴⁺ peak at 487.4 eV was observed, while CsSn_{0.6}Ge_{0.4}I₃ remained stable. The stability of CsSn_{0.6}Ge_{0.4}I₃ is higher with t = 0.90 as compared to its Sn counterpart (t = 0.84), suggesting that involvement of Ge²⁺ cation leads to better stability and even barrier for the infiltration of moisture. Ge²⁺ cation helps to protect Sn²⁺ cation in alloy system and suppresses further oxidation of Sn²⁺ (Fig. 9(b)) [90]. Photophysical study further validated the mechanism of filling effect of Ge²⁺ cation in CsSn_{0.6}Ge_{0.4}I₃ perovskite NCs, where the quenching time is extended from 490 ps and 4200 ps, with PCE of 4.9% (Fig. 9(c-d)). Ethylenediamine (EDA) not only contributes to the surface passivation, but it also contributes to the stability enhancement of Sn perovskites. Chen et al. reported the device stability of (GA_{0.06}(FA_{0.8}Cs_{0.2})_{0.94})_{0.98}SnI₂Br with 3% GeI₂ increased with the addition of EDA (EDA_{0.10}) surface passivator. Also retaining 80% of device efficiency even after 25 days kept without encapsulation in N₂ atmosphere was found (Fig. 9(e)) [74]. Incorporating hydrophobic organic cations can help in maintaining perovskite stability by restricting moisture penetration because it either leads to the formation of 2D/3D bilayer or 2D/3D heterostructure.

Replacement of Li-salt doped Spiro-OMeTAD with hydrophobic p-type conjugated polymer poly[(5-fluoro-2,1,3-benzothiadiazole-4,7-

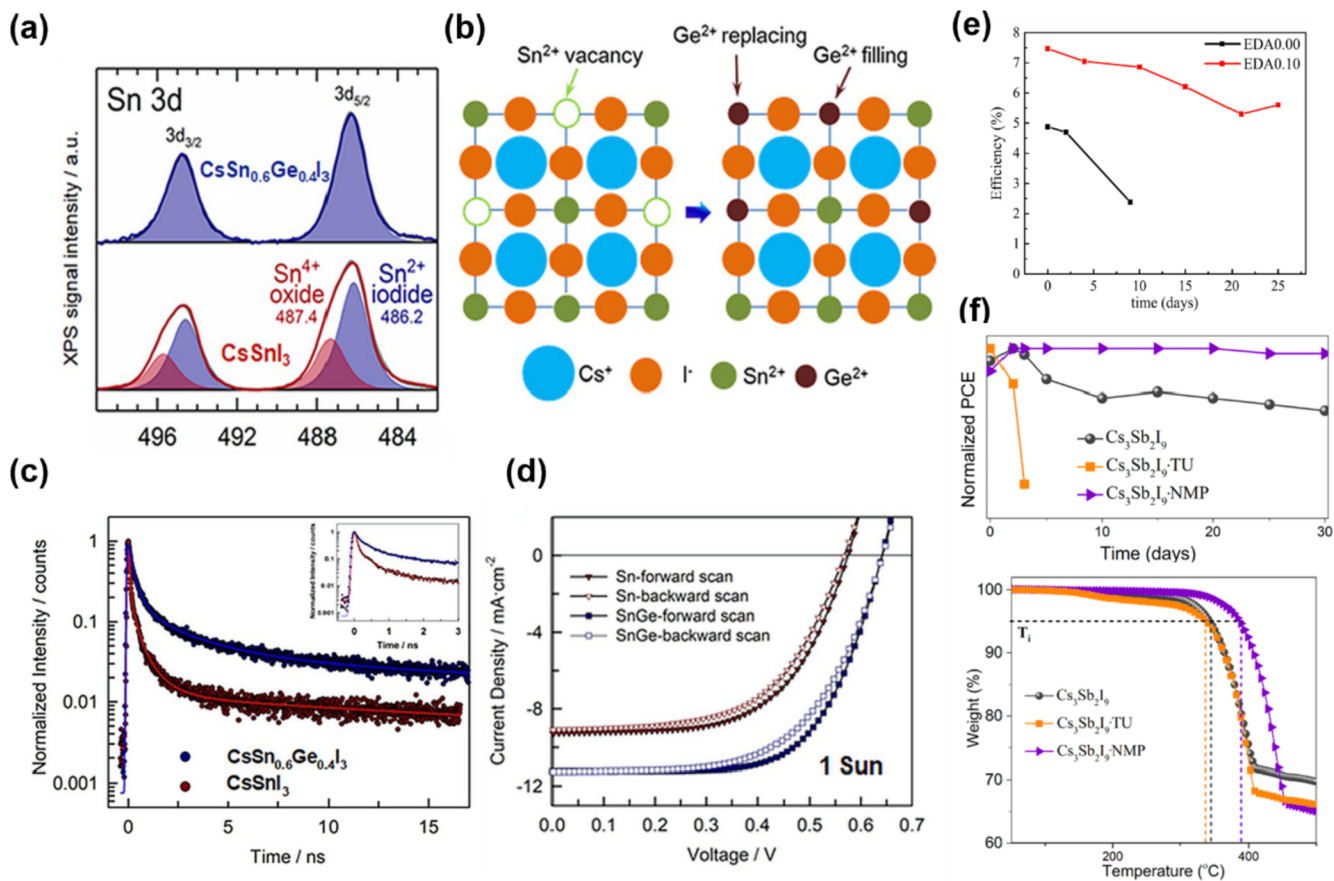


Fig. 9. (a) Comparative XPS core spectra of Sn 3d transition states for $\text{CsSn}_{0.6}\text{Ge}_{0.4}\text{I}_3$ and CsSnI_3 NCs after 10 min air exposure, (b) Representation of Ge filling effect within Sn vacant states and the substitution of Sn through Ge atoms, (c) TRPL decay curve and (d) J-V characteristics for CsSnI_3 and $\text{CsSn}_{0.6}\text{Ge}_{0.4}\text{I}_3$ PSCs. Reproduced under the terms of Creative Commons CC BY license. Copyright (2020) [90]. (e) Stability comparison data for EDA0.10 and EDA0 with respect to the storage time of 25 days. Reproduced with permission from Elsevier. Copyright (2022) [74]. (f) Long term stability comparison over 30 days and thermogravimetric analysis (TGA) of controlled $\text{Cs}_3\text{Sb}_2\text{I}_9$ with $\text{Cs}_3\text{Sb}_2\text{I}_9$ -NMP and $\text{Cs}_3\text{Sb}_2\text{I}_9$ -TU. Reproduced with permission from American Chemical Society. Copyright (2020) [79].

diyl)(4,4-dihexadecyl-4H-cyclopenta[2,1-b:3,4-b']dithiophene-2,6-diyl)(6-fluoro-2,1,3-benzothiadiazole-4,7-diyl)(4,4-dihexadecyl-4H-cyclopenta[2,1-b:3,4-b']dithiophene-2,6-diyl]) (PCDTFBT) as a HTL in $\text{Cs}_2\text{AgBiBr}_6$ planar n-i-p device not only provides efficient hole extraction due to proper band alignment with $\text{Cs}_2\text{AgBiBr}_6$, but it also enhanced environmental and light stability of device over 120 h [91]. $\text{Cs}_3\text{Sb}_2\text{I}_9$ layered perovskite polymorph with direct $E_g \sim 2.0$ eV as compared to 0D phase (indirect $E_g \sim 2.50$ eV) is speculated to be an efficient photo-absorber in PSCs with high operational stability [77]. HCl additive assisted perovskite growth forms pure phase layered perovskite where the operational stability of more than 50 h in ambient atmospheric condition was observed. Detailed analysis revealed that trap densities significantly reduced from 5.19×10^{15} (0D) to $1.10 \times 10^{15} \text{ cm}^{-3}$ for layered $\text{Cs}_3\text{Sb}_2\text{I}_9$ with enhancement in carrier mobility to $6.81 \text{ cm}^2\text{V}^{-1}\text{s}^{-1}$ and thermal stability. Long term device stability over 30 days under N_2 atmosphere was also observed for D- $\text{Cs}_3\text{Sb}_2\text{I}_9$ WBG PSC. It has been observed that formation of Lewis acid base adducts of $\text{CsI/Sb}_3\text{I}_9$ -DMF-DMSO precursor solution with NMP or thiourea (TU) leads to the formation of adduct complex which controls crystallization rate. Thermal stability was studied using thermogravimetric analysis (Fig. 9(f)), where the initial dip was observed at 150 °C for $\text{Cs}_3\text{Sb}_2\text{I}_9$ -TU. On the other hand, $\text{Cs}_3\text{Sb}_2\text{I}_9$ -NMP film experienced no decomposition up to 350 °C, indicating high operational and thermal stability of $\text{Cs}_3\text{Sb}_2\text{I}_9$ -NMP PSC [79].

5. Conclusion and prospects

The PCE enhancement in TSCs is highly demanding, as photo-

absorbers with suitable bandgaps in TSCs stack together that efficiently harness maximum solar radiation by reducing thermalization loss. The selection of photo-absorber in a particular range of bandgap is very crucial specially for 2T-TSCs. The photons of short wavelengths are absorbed through WBG front sub-cell, which delivers high V_{oc} in TSCs. Under constant research and development Pb-OIHPs are near to approach S-Q limit for SJ solar cells, although Pb-toxicity and operational instability over time needs replacement of Pb which is highly demanding from eco-friendly prospect. By understanding the serious issue, in the present review we have systematically discussed the existing challenges and issues related to Pb-free WBG perovskites in terms of fast crystallization, defect formation, instability, and the ways followed hitherto to overcome these issues and enhance PCE in Pb-free WBG PSCs. In our knowledge, this review is critical in that it will accelerate more research efforts in developing Pb-free WBG PSC technology towards high efficiency achievement. Hence based on existing technological developments and above discussions, we conclude here with a perspective that might be useful to a broad readership to enhance Pb-free WBG PSCs efficiency and their application in TSCs, which is highly challenging to be achieved. Schematic illustration (Fig. 10) depicts the development of high quality Pb-free WBG perovskite by following multiple strategies and enlightening the major challenges that requires focused efforts.

1. High performance device. The PCE in Pb-free WBG PSCs is not satisfactorily high as compared to its Pb counterpart. Hence for further boosting the efficiency, it is crucial to focus collectively on all the factors such as J_{sc} , V_{oc} and FF of the device.

J_{sc} and V_{oc} enhancement. The reduced J_{sc} in Pb-free WBG PSCs is

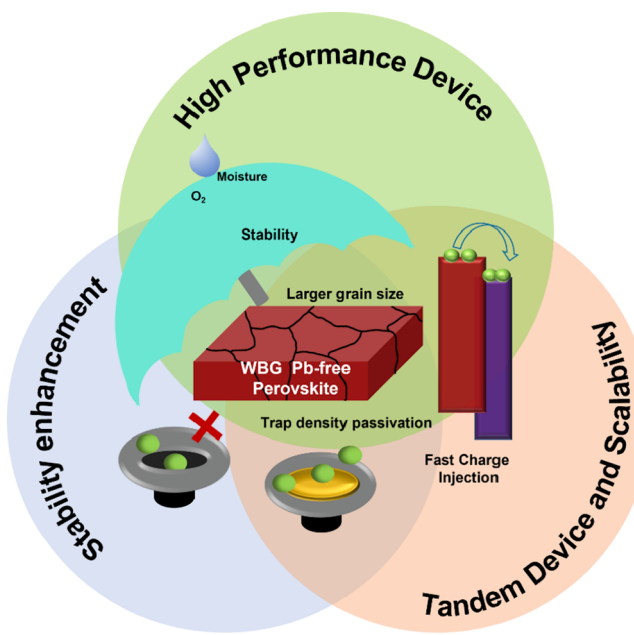


Fig. 10. Graphical illustration proposing future high performance Pb-free WBG perovskite device technology evolving through multiple defect passivation strategies and relationship with device stability, scalability and developing TSCs.

one of the major parameters, which should be further reinforced for achieving high performance in WBG PSCs. For instance, in Sn WBG perovskites, it is suggested to focus more on film crystallinity and carrier diffusion lengths, while more strategic advancement is needed to fabricate highly uniform and smooth film for Bi and Sb WBG perovskites. The thickness of perovskite absorber is a significant parameter for efficient charge carrier generation. In the case of Sn PSCs, the J_{sc} increases with increasing film thickness from 100 to 175 nm, which shows drop in J_{sc} and V_{oc} with gradual increase in film thickness to 200–250 nm. This indicates short diffusion length in 200–250 nm thick perovskite film [92]. Hence, we expect that prolonged carrier diffusion length within perovskite film will be critical for better charge transport properties and can further enhance the J_{sc} . Proper combinations in compositional, additive engineering as well as solution/vacuum processing might further enhance film crystallinity of Sn-based perovskites with less defects formation. The study on WBG Pb-free PSCs is still at initial stage, hence the newly developed, specific materials and processing to control perovskite grain growth needs to be further integrated as a single processing.

As for Bi or Sb based perovskites, they have appropriate WBGs with comparatively less V_{oc} deficit compared to the case of Sn based analogues. However, intrinsic defects form due to rapid crystallization and uncontrolled growth that leads to poor morphology, which severely hampers the charge transport properties of device and reduce J_{sc} . Hence, regulation of crystal growth and proper grain size can be an essential approach. Furthermore, it is believed that grain engineering strategies such as improving grain size with preferential orientation and reducing surface/bulk defects by introducing additives, ionic liquids, or surface passivating layers, will be useful to develop highly uniform Pb-free WBG perovskite film. In addition, the conductivity of perovskite can be further enhanced by introducing pseudohalide ions in Pb-free WBG perovskites. Insertion of charge extraction layers may benefit to enhance the charge extraction processes such as carbides/nitrides owing to their surface functionalities and high surface area. By increasing overall conductivity in perovskites and controlling crystal growth, these kinds of strategies might be advantageous in enhancing PCE in Pb-free WBG PSCs.

Reduce V_{oc} deficits. In addition, to achieve high performance WBG PSCs, it needs to critically focus on V_{oc} enhancement strategies. As

compared to Pb PSCs, Pb-free PSCs suffers from V_{oc} deficits, which is ascribed to the intrinsic defects and band level mismatch. Fabricating high quality perovskite film may reduce the intrinsic defects, increase recombination lifetime by passivating bulk defects, which can be achieved by introducing organic cations and molecules for passivation. Additionally, poor band alignments of WBG perovskites with CTls results in V_{oc} deficits. We suppose this can be resolved by opting following strategies such as (i) Cation compositional engineering in Pb-free WBG perovskites with organic molecules, which leads to either constructing bilayer or quasi 2D/3D perovskites. It can further facilitate desirable CB upshift that can match well with CTL due to quantum confinement effect of 2D perovskites. (ii) Doping CTL with traces of small molecules can further help in tuning the band energy levels. (iii) Interfacial modification between perovskite/ETL using self-assemble molecules (SAMs) can be beneficial to enhance the molecular coupling and tune the energy levels.

2. Stability enhancement.

Bi and Sb WBG perovskite are more robust under constant device operation and light illumination than Sn WBG perovskites. However, till now these (Bi or Sb) perovskites are not capable to deliver high device performance due to poor J_{sc} . On the other hand, environmental/thermal instability brings extra limitation for the long-term utilization of Sn WBG PSCs. Further research need to be conducted in this direction by introducing hydrophobic organic ligands like ethylenediamine, propylamine, or phenylethylamine etc. for 2D/3D perovskite which helps in reducing moisture penetration, photo-degradation and improving the stability of Pb-free WBG perovskites.

3. Tandem device and scalability.

The overall efficiency enhancement in Pb-free WBG PSCs is essential as it can be further utilized as front sub-cells in non-toxic perovskite TSCs to maximize the PCEs. In addition, for further commercialization point of view, one needs to focus on developing large area devices which is of equal importance. Since the already established solution processing techniques are not suitable enough to develop large area perovskite film with high uniformity, hence it is essential to develop new strategies of utilizing deposition units such as thermal evaporation for such Pb-free WBG perovskites. Also as a solution approach, establishing slot die, doctor blading, roll to roll method and etc. for homogenous and large area perovskite film fabrication will be required. The given perspective will be helpful in providing more clarity and innovative ideas for broad scientific reader and paving a way in future advancement in efficiencies of Pb-free WBG PSCs. The future device technology should be progressed eco-friendly and hence we have targeted to provide this extensive information that can be helpful to overcome the existing challenges. Though it is difficult to bring Pb-free device technology to commercial level in current status, we speculate that the current awareness and enormous efforts may push it to next level on technological grounds.

Declaration of Competing Interest

The authors declare that they have no known competing financial interests or personal relationships that could have appeared to influence the work reported in this paper.

Data availability

Data will be made available on request.

Acknowledgements

We would like to acknowledge National Research Foundation of Korea, funded by the Korea government (MSIT) (NRF-2021R1A2C4002045, 2021R1A4A2001687, and 2021K2A9A2A08000082).

Appendix A. Supplementary data

Supplementary data to this article can be found online at <https://doi.org/10.1016/j.cej.2022.137622>.

References

- [1] I. Dincer, Renewable energy and sustainable development: a crucial review, *Renew. Sust. Energ. Rev.* 4 (2) (2000) 157–175, <https://doi.org/10.1038/d41586-019-01985-y>.
- [2] A. Extance, The reality behind solar power's next star material, *Nature* 570 (7762) (2019) 429–433, <https://doi.org/10.1038/d41586-019-01985-y>.
- [3] A. Richter, J. Benick, F. Feldmann, A. Fell, M. Hermle, S.W. Glunz, n-Type Si solar cells with passivating electron contact: Identifying sources for efficiency limitations by wafer thickness and resistivity variation, *Sol. Energy Mater. Sol. Cells* 173 (2017) 96–105, <https://doi.org/10.1016/j.solmat.2017.05.042>.
- [4] H. Min, D.Y. Lee, J. Kim, G. Kim, K.S. Lee, J. Kim, M.J. Paik, Y.K. Kim, K.S. Kim, M.G. Kim, T.J. Shin, S. Il Seok, Perovskite solar cells with atomically coherent interlayers on SnO₂ electrodes, *Nature* 598 (7881) (2021) 444–450, <https://doi.org/10.1038/s41586-021-03964-8>.
- [5] X. Luo, T. Wu, Y. Wang, X. Lin, H. Su, Q. Han, L. Han, Progress of all-perovskite tandem solar cells: the role of narrow-bandgap absorbers, *Sci. China Chem.* 64 (2) (2021) 218–227, <https://doi.org/10.1007/s11426-020-9870-4>.
- [6] S. Albrecht, M. Saliba, J.P. Correa Baena, F. Lang, L. Kegelmann, M. Mews, L. Steier, A. Abate, J. Rappich, L. Korte, R. Schlatmann, M.K. Nazeeruddin, A. Hagfeldt, M. Grätzel, B. Rech, Monolithic perovskite/silicon-heterojunction tandem solar cells processed at low temperature, *Energy Environ. Sci.* 9 (1) (2016) 81–88, <https://doi.org/10.1039/C5EE02965A>.
- [7] J. Werner, A. Walter, E. Rucavado, S.-J. Moon, D. Sacchetto, M. Riennaeker, R. Peibst, R. Brendel, X. Niquille, S. De Wolf, P. Löper, M. Morales-Masis, S. Nicolay, B. Niesen, C. Ballif, Zinc tin oxide as high-temperature stable recombination layer for mesoscopic perovskite/silicon monolithic tandem solar cells, *Appl. Phys. Lett.* 109 (23) (2016), 233902, <https://doi.org/10.1063/1.4971361>.
- [8] R. He, S. Ren, C. Chen, Z. Yi, Y. Luo, H. Lai, W. Wang, G. Zeng, X. Hao, Y. Wang, J. Zhang, C. Wang, L. Wu, F. Fu, D. Zhao, Wide-bandgap organic–inorganic hybrid and all-inorganic perovskite solar cells and their application in all-perovskite tandem solar cells, *Energy Environ. Sci.* 14 (11) (2021) 5723–5759, <https://doi.org/10.1039/DIEE01562A>.
- [9] T. Leijtens, K.A. Bush, R. Prasanna, M.D. McGehee, Opportunities and challenges for tandem solar cells using metal halide perovskite semiconductors, *Nat. Energy* 3 (10) (2018) 828–838, <https://doi.org/10.1038/s41560-018-0190-4>.
- [10] Z. Fang, Q. Zeng, C. Zuo, L. Zhang, H. Xiao, M. Cheng, F. Hao, Q. Bao, L. Zhang, Y. Yuan, W.-Q. Wu, D. Zhao, Y. Cheng, H. Tan, Z. Xiao, S. Yang, F. Liu, Z. Jin, J. Yan, L. Ding, Perovskite-based tandem solar cells, *Sci. Bull.* 66 (6) (2021) 621–636, <https://doi.org/10.1016/j.scib.2020.11.006>.
- [11] H. Li, W. Zhang, Perovskite tandem solar cells: from fundamentals to commercial deployment, *Chem. Rev.* 120 (18) (2020) 9835–9950, <https://doi.org/10.1021/acs.chemrev.9b00780>.
- [12] R. Nie, R.R. Sumukam, S.H. Reddy, M. Banavoth, S.I. Seok, Lead-free perovskite solar cells enabled by hetero-valent substitutes, *Energy Environ. Sci.* 13 (8) (2020) 2363–2385, <https://doi.org/10.1039/D0EE01153C>.
- [13] B. Chen, C. Fei, S. Chen, H. Gu, X. Xiao, J. Huang, Recycling lead and transparent conductors from perovskite solar modules, *Nat. Commun.* 12 (1) (2021) 1–10, <https://doi.org/10.1038/s41467-021-26121-1>.
- [14] Y. Jiang, L. Qiu, E.J. Juarez-Perez, L.K. Ono, Z. Hu, Z. Liu, Z. Wu, L. Meng, Q. Wang, Y. Qi, Reduction of lead leakage from damaged lead halide perovskite solar modules using self-healing polymer-based encapsulation, *Nat. Energy* 4 (7) (2019) 585–593, <https://doi.org/10.1038/s41560-019-0406-2>.
- [15] J. Li, J. Duan, X. Yang, Y. Duan, P. Yang, Q. Tang, Review on recent progress of lead-free halide perovskites in optoelectronic applications, *Nano Energy* 80 (2021), 105526, <https://doi.org/10.1016/j.nanoen.2020.105526>.
- [16] A. Goyal, S. McKechnie, D. Pashov, W. Tumas, M. Van Schilfgaarde, V. Stevanovic, Origin of pronounced nonlinear band gap behavior in lead–tin hybrid perovskite alloys, *Chem. Mater.* 30 (11) (2018) 3920–3928, <https://doi.org/10.1021/acs.chemmater.8b01695>.
- [17] Y. Li, W. Sun, W. Yan, S. Ye, H. Rao, H. Peng, Z. Zhao, Z. Bian, Z. Liu, H. Zhou, C. Huang, 50% Sn-based planar perovskite solar cell with power conversion efficiency up to 13.6%, *Adv. Energy Mater.* 6 (24) (2016) 1601353, <https://doi.org/10.1002/aenm.201601353>.
- [18] N. Aristidou, C. Eames, I. Sanchez-Molina, X. Bu, J. Kosco, M.S. Islam, S.A. Haque, Fast oxygen diffusion and iodide defects mediate oxygen-induced degradation of perovskite solar cells, *Nat. Commun.* 8 (1) (2017) 1–10, <https://doi.org/10.1038/ncomms15218>.
- [19] E.J. Juarez-Perez, L.K. Ono, M. Maeda, Y. Jiang, Z. Hawash, Y. Qi, Photodecomposition and thermal decomposition in methylammonium halide lead perovskites and inferred design principles to increase photovoltaic device stability, *J. Mater. Chem. A* 6 (20) (2018) 9604–9612, <https://doi.org/10.1039/C8TA03501F>.
- [20] L. Lanzetta, N. Aristidou, S.A. Haque, Stability of lead and tin halide perovskites: the link between defects and degradation, *J. Phys. Chem. Lett.* 11 (2) (2020) 574–585, <https://doi.org/10.1021/acs.jpclett.9b02191>.
- [21] Z. Wang, Y. Wang, Z. Nie, Y. Ren, H. Zeng, Laser induced ion migration in all-inorganic mixed halide perovskite micro-platelets, *Nanoscale Adv.* 1 (11) (2019) 4459–4465, <https://doi.org/10.1039/C9NA00565J>.
- [22] D. Meggiolaro, E. Mosconi, F. De Angelis, Formation of surface defects dominates ion migration in lead-halide perovskites, *ACS Energy Lett.* 4 (3) (2019) 779–785, <https://doi.org/10.1021/acsenergylett.9b00247>.
- [23] R. Gorkhal, K. Huang, M. Kirberger, J.J. Yang, Defining potential roles of Pb²⁺ in neurotoxicity from a calciumics approach, *Metalloomics* 8 (6) (2016) 563–578, <https://doi.org/10.1039/c6mt00038j>.
- [24] G. Schileo, G. Grancini, Lead or no lead? Availability, toxicity, sustainability and environmental impact of lead-free perovskite solar cells, *J. Mater. Chem. C* 9 (1) (2021) 67–76, <https://doi.org/10.1039/DTOC4552G>.
- [25] J. Li, H.-L. Cao, W.-B. Jiao, Q. Wang, M. Wei, I. Cantone, J. Liu, A. Abate, Biological impact of lead from halide perovskites reveals the risk of introducing a safe threshold, *Nat. Commun.* 11 (1) (2020) 1–5, <https://doi.org/10.1038/s41467-019-13910-y>.
- [26] X.-G. Zhao, D. Yang, J.-C. Ren, Y. Sun, Z. Xiao, L. Zhang, Rational design of halide double perovskites for optoelectronic applications, *Joule* 2 (9) (2018) 1662–1673, <https://doi.org/10.1016/j.joule.2018.06.017>.
- [27] D. Moghe, L. Wang, C.J. Traverse, A. Redoute, M. Sponseller, P.R. Brown, V. Bulović, R.R. Lunt, All vapor-deposited lead-free doped CsSnBr 3 planar solar cells, *Nano Energy* 28 (2016) 469–474, <https://doi.org/10.1016/j.nanoen.2016.09.009>.
- [28] S. Gupta, T. Bendikov, G. Hodes, D. Cahen, CsSnBr 3, a lead-free halide perovskite for long-term solar cell application: insights on SnF₂ addition, *ACS Energy Lett.* 1 (5) (2016) 1028–1033, <https://doi.org/10.1021/acsenergylett.6b00402>.
- [29] F. Hao, C.C. Stoumpos, D.H. Cao, R.P. Chang, M.G. Kanatzidis, Lead-free solid-state organic–inorganic halide perovskite solar cells, *Nat. Photonics* 8 (6) (2014) 489–494, <https://doi.org/10.1038/nphoton.2014.82>.
- [30] D. Song, L.Y. Hsu, C.-M. Tseng, E.-W.-G. Diau, Solution-processed ITO nanoparticles as hole-selective electrodes for mesoscopic lead-free perovskite solar cells, *Mater. Adv.* 2 (2) (2021) 754–759, <https://doi.org/10.1039/DOMA00860E>.
- [31] M. Zhang, M. Lyu, J.-H. Yun, M. Noori, X. Zhou, N.A. Cooling, Q. Wang, H. Yu, P. C. Dastoor, L. Wang, Low-temperature processed solar cells with formamidinium tin halide perovskite/fullerene heterojunctions, *Nano Res.* 9 (6) (2016) 1570–1577, <https://doi.org/10.1007/s12274-016-1051-8>.
- [32] J.-J. Cao, Y.-H. Lou, W.-F. Yang, K.-L. Wang, Z.-H. Su, J. Chen, C.-H. Chen, C. Dong, X.-Y. Gao, Z.-K. Wang, Multifunctional potassium thiocyanate interlayer for eco-friendly tin perovskite indoor and outdoor photovoltaics, *Chem. Eng. J.* 433 (2022), 133832, <https://doi.org/10.1016/j.cej.2021.133832>.
- [33] T. Shi, H.-S. Zhang, W. Meng, Q. Teng, M. Liu, X. Yang, Y. Yan, H.-L. Yip, Y.-J. Zhao, Effects of organic cations on the defect physics of tin halide perovskites, *J. Mater. Chem. A* 5 (29) (2017) 15124–15129, <https://doi.org/10.1039/C7TA02662E>.
- [34] W. Ke, C.C. Stoumpos, M.G. Kanatzidis, “Unleaded” perovskites: status quo and future prospects of tin-based perovskite solar cells, *Adv. Mater.* 31 (47) (2019) 1803230, <https://doi.org/10.1002/adma.201803230>.
- [35] B.P. Nguyen, D. Shin, H.R. Jung, J. Kim, T.T.T. Nguyen, S. Yoon, Y. Yi, W. Jo, Phase formation and local charge transport of lead-free CH₃NH₃Sn (11–xBr_x)₃ (0 ≤ x ≤ 1) perovskite solar cells fabricated by solvent optimization, *Sol. Energy* 186 (2019) 136–144, <https://doi.org/10.1016/j.solener.2019.05.007>.
- [36] E. Jokar, C.H. Chien, C.M. Tsai, A. Fathi, E.W.G. Diau, Robust tin-based perovskite solar cells with hybrid organic cations to attain efficiency approaching 10%, *Adv. Mater.* 31 (2) (2019) 1804835, <https://doi.org/10.1002/adma.201804835>.
- [37] M. Chen, G. Kapil, L. Wang, S. Razey Sahamir, A.K. Baranwal, K. Nishimura, Y. Sanehira, Z. Zhang, M. Akmal Kamarudin, Q. Shen, S. Hayase, High performance wide bandgap Lead-free perovskite solar cells by monolayer engineering, *Chem. Eng. J.* 436 (2022), 135196, <https://doi.org/10.1016/j.cej.2022.135196>.
- [38] G.-X. Liang, X.-Y. Chen, Z.-H. Chen, H.-B. Lan, Z.-H. Zheng, P. Fan, X.-Q. Tian, J.-Y. Duan, Y.-D. Wei, Z.-H. Su, Inorganic and Pb-free CsBi₃I₁₀ thin film for photovoltaic applications, *J. Phys. Chem. C* 123 (45) (2019) 27423–27428, <https://doi.org/10.1021/acs.jpcc.9b09617>.
- [39] S.M. Jain, T. Edvinsson, J.R. Durrant, Green fabrication of stable lead-free bismuth based perovskite solar cells using a non-toxic solvent, *Commun. Chem.* 2 (1) (2019) 1–7, <https://doi.org/10.1038/s42004-019-0195-3>.
- [40] D.B. Khadka, Y. Shirai, M. Yanagida, K. Miyano, Tailoring the film morphology and interface band offset of caesium bismuth iodide-based Pb-free perovskite solar cells, *J. Mater. Chem. C* 7 (27) (2019) 8335–8343, <https://doi.org/10.1039/C9TC02181G>.
- [41] J. Zhou, F. Zhao, J. Shen, Y. Zhou, Y. Wu, Y. Guo, J. Jiang, J. Chu, Inorganic lead-free antimony-based perovskite-inspired solar cells with a carbon electrode and green anti-solvent regulation, *J. Mater. Chem. C* 9 (42) (2021) 15301–15308, <https://doi.org/10.1039/D1TC03885K>.
- [42] F. Li, Y. Wang, X. Xia, R.L. Hoye, V. Pecunia, Microstructural and photoconversion efficiency enhancement of compact films of lead-free perovskite derivative Rb 3 Sb 2 I 9, *J. Mater. Chem. A* 8 (8) (2020) 4396–4406, <https://doi.org/10.1039/C9TA13352F>.
- [43] E. Jokar, H.-S. Chuang, C.-H. Kuan, H.-P. Wu, C.-H. Hou, J.-J. Shyue, E. Wei-Guang Diau, Slow passivation and inverted hysteresis for hybrid tin perovskite solar cells attaining 13.5% via sequential deposition, *J. Phys. Chem. Lett.* 12 (41) (2021) 10106–10111.
- [44] E. Jokar, P.-Y. Cheng, C.-Y. Lin, S. Narra, S. Shahbazi, E. Wei-Guang Diau, Enhanced performance and stability of 3D/2D tin perovskite solar cells fabricated with a sequential solution deposition, *ACS Energy Lett.* 6 (2) (2021) 485–492, <https://doi.org/10.1021/acsenergylett.6c02305>.

- [45] T. Yokoyama, T.-B. Song, D.H. Cao, C.C. Stoumpos, S. Aramaki, M.G. Kanatzidis, The origin of lower hole carrier concentration in methylammonium tin halide films grown by a vapor-assisted solution process, *ACS Energy Lett.* 2 (1) (2017) 22–28, <https://doi.org/10.1021/acsenergylett.6b00513>.
- [46] M.-C. Jung, S.R. Raga, Y. Qi, Properties and solar cell applications of Pb-free perovskite films formed by vapor deposition, *RSC Adv.* 6 (4) (2016) 2819–2825, <https://doi.org/10.1039/C5RA21291J>.
- [47] S.M. Jain, D. Phuyal, M.L. Davies, M. Li, B. Philippe, C. De Castro, Z. Qiu, J. Kim, T. Watson, W.C. Tsoi, O. Karis, H. Rensmo, G. Boschloo, T. Edvinsson, J.R. Durrant, An effective approach of vapour assisted morphological tailoring for reducing metal defect sites in lead-free, (CH_3NH_3) $3\text{Bi}_2\text{I}_9$ bismuth-based perovskite solar cells for improved performance and long-term stability, *Nano Energy* 49 (2018) 614–624, <https://doi.org/10.1016/j.nanoen.2018.05.003>.
- [48] B.W. Park, B. Philippe, X. Zhang, H. Rensmo, G. Boschloo, E.M. Johansson, Bismuth based hybrid perovskites $\text{A}3\text{Bi}_2\text{I}_9$ (A : methylammonium or cesium) for solar cell application, *Adv. Mater.* 27 (43) (2015) 6806–6813, <https://doi.org/10.1002/adma.201501978>.
- [49] J. Li, X. Liu, J. Xu, J. Chen, C. Zhao, M. Salma Maneno, B. Zhang, J. Yao, Fabrication of sulfur-incorporated bismuth-based perovskite solar cells via a vapor-assisted solution process, *Sol. RRL* 3 (9) (2019) 1900218, <https://doi.org/10.1002/solr.201900218>.
- [50] D. Fang, Y. Tong, F. Xu, B. Mi, D. Cao, Z. Gao, Preparation of CsSnBr_3 perovskite film and its all-inorganic solar cells with planar heterojunction, *J. Solid State Chem.* 294 (2021), 121902, <https://doi.org/10.1016/j.jssc.2020.121902>.
- [51] R. Prasanna, A. Gold-Parker, T. Leijtens, B. Conings, A. Babayigit, H.-G. Boyen, M.F. Toney, M.D. McGehee, Band gap tuning via lattice contraction and octahedral tilting in perovskite materials for photovoltaics, *J. Am. Chem. Soc.* 139 (32) (2017) 11117–11124, <https://doi.org/10.1021/jacs.7b04981>.
- [52] W. Ke, C.C. Stoumpos, M. Zhu, L. Mao, I. Spanopoulos, J. Liu, O.Y. Kontsevoi, M. Chen, D. Sarma, Y. Zhang, M.R. Wasielewski, M.G. Kanatzidis, Enhanced photovoltaic performance and stability with a new type of hollow 3D perovskite en FASnI_3 , *Sci. Adv.* 3 (8) (2017) e1701293, <https://doi.org/10.1126/sciadv.1701293>.
- [53] C.-M. Tsai, Y.-P. Lin, M.K. Pola, S. Narra, E. Jokar, Y.-W. Yang, E.-W.-G. Diau, Control of crystal structures and optical properties with hybrid formamidinium and 2-hydroxyethylammonium cations for mesoscopic carbon-electrode tin-based perovskite solar cells, *ACS Energy Lett.* 3 (9) (2018) 2077–2085, <https://doi.org/10.1021/acsenergylett.8b01046>.
- [54] M. Chen, M.A. Kamarudin, A.K. Baranwal, G. Kapil, T.S. Ripolles, K. Nishimura, D. Hirotani, S.R. Sahamir, Z. Zhang, C. Ding, Y. Sanechira, J. Bisquert, Q. Shen, S. Hayase, High-efficiency lead-free wide band gap perovskite solar cells via guanidinium bromide incorporation, *ACS Appl. Energy Mater.* 4 (6) (2021) 5615–5624, <https://doi.org/10.1021/acssem.1c00413>.
- [55] T. Krishnamoorthy, H. Ding, C. Yan, W.L. Leong, T. Baikie, Z. Zhang, M. Sherburne, S. Li, M. Asta, N. Mathews, S.G. Mhaisalkar, Lead-free germanium iodide perovskite materials for photovoltaic applications, *J. Mater. Chem. A* 3 (47) (2015) 23829–23832, <https://doi.org/10.1039/C5TA05741H>.
- [56] I. Kopacic, B. Friesenbichler, S.F. Hoefler, B. Kunert, H. Plank, T. Rath, G. Trimmel, Enhanced performance of germanium halide perovskite solar cells through compositional engineering, *ACS Appl. Energy Mater.* 1 (2) (2018) 343–347, <https://doi.org/10.1021/acssem.8b00007>.
- [57] J. Li, J. Duan, J. Du, X. Yang, Y. Wang, P. Yang, Y. Duan, Q. Tang, Alkali metal ion-regulated lead-free, all-inorganic double perovskites for HTM-free, carbon-based solar cells, *ACS Appl. Mater. Interfaces* 12 (42) (2020) 47408–47415, <https://doi.org/10.1021/acsami.0c11770>.
- [58] A. Maiti, A.J. Pal, Effect of cation occupancy ordering in double perovskites to overcome hurdles in carrier transport: $\text{Cs}_2\text{AgBiBr}_6$ as a case study, *J. Phys. Chem. C* 125 (29) (2021) 16324–16333, <https://doi.org/10.1021/acs.jpcc.1c04730>.
- [59] Y. Guo, J. Zhou, F. Zhao, Y. Wu, J. Tao, S. Zuo, J. Jiang, Z. Hu, J. Chu, Carbon-based 2D-layered $\text{Rb}_0.15\text{Cs}_2.85\text{Sb}_2\text{ClxI}_{9-x}$ solar cells with superior open-voltage up to 0.88 V, *Nano Energy* 88 (2021) 106281, <https://doi.org/10.1016/j.nanoen.2021.106281>.
- [60] D. Sabba, H.K. Mulumudi, R.R. Prabhakar, T. Krishnamoorthy, T. Baikie, P.P. Boix, S. Mhaisalkar, N. Mathews, Impact of anionic Br-substitution on open circuit voltage in lead free perovskite ($\text{CsSnI}_3\text{-xBr x}$) solar cells, *J. Phys. Chem. C* 119 (4) (2015) 1763–1767, <https://doi.org/10.1021/jp5126624>.
- [61] B. Lee, A. Krenselewski, S.I. Baik, D. Seidman, R. Chang, PH Solution processing of air-stable molecular semiconducting iodosalts, $\text{Cs}_2\text{SnI}_6\text{-xBr x}$, for potential solar cell applications, *Sustain. Energy Fuels* 1 (4) (2017) 710–724, <https://doi.org/10.1039/C7SE00100B>.
- [62] S.J. Lee, S.S. Shin, J. Im, T.K. Ahn, J.H. Noh, N.J. Jeon, S.I. Seok, J. Seo, Reducing carrier density for formamidinium tin perovskites and its beneficial effects on stability and efficiency of perovskite solar cells, *ACS Energy Lett.* 3 (1) (2017) 46–53, <https://doi.org/10.1021/acsenergylett.7b000976>.
- [63] C.M. Tsai, N. Mohanta, C.Y. Wang, Y.P. Lin, Y.W. Yang, C.L. Wang, C.H. Hung, E.W.G. Diau, Formation of stable tin perovskites co-crystallized with three halides for carbon-based mesoscopic lead-free perovskite solar cells, *Angew. Chem. Int. Ed.* 56 (44) (2017) 13819–13823, <https://doi.org/10.1002/anie.201707037>.
- [64] H. Li, X. Jiang, Q. Wei, Z. Zang, M. Ma, F. Wang, W. Zhou, Z. Ning, Low-dimensional inorganic tin perovskite solar cells prepared by templated growth, *Angew. Chem. Int. Ed.* 60 (30) (2021) 16330–16336, <https://doi.org/10.1002/anie.202104958>.
- [65] B.-B. Yu, M. Liao, J. Yang, W. Chen, Y. Zhu, X. Zhang, T. Duan, W. Yao, S.-H. Wei, Z. He, Alloy-induced phase transition and enhanced photovoltaic performance: the case of $\text{Cs}_3\text{Bi}_2\text{I}_9\text{-xBr x}$ perovskite solar cells, *J. Mater. Chem. A* 7 (15) (2019) 8818–8825, <https://doi.org/10.1039/C9TA01978B>.
- [66] X. Zhang, X. Liu, R. Yan, J. Yang, Y. Liu, S. Dong, Ion-assisted self-assembly of macroporous MXene films as supercapacitor electrodes, *J. Mater. Chem. C* 8 (6) (2020) 2008–2013, <https://doi.org/10.1039/C9TC05595A>.
- [67] G. Paul, A.J. Pal, B.W. Larson, Structure, morphology, and photovoltaic implications of halide alloying in lead-free $\text{Cs}_3\text{Sb}_2\text{ClxI}_{9-x}$ 2D-Layered perovskites, *Sol. RRL* 5 (1) (2021) 2000422, <https://doi.org/10.1002/solr.202000422>.
- [68] M. Xiao, S. Gu, P. Zhu, M. Tang, W. Zhu, R. Lin, C. Chen, W. Xu, T. Yu, J. Zhu, Tin-based perovskite with improved coverage and crystallinity through tin-fluoride-assisted heterogeneous nucleation, *Adv. Opt. Mater.* 6 (1) (2018) 1700615, <https://doi.org/10.1002/adom.201700615>.
- [69] C. Hartmann, S. Gupta, T. Bendikov, X. Kozina, T. Kunze, R. Felix, G. Hodes, R. Wilks, D. Cahen, M. Bar, Impact of SnF_2 addition on the chemical and electronic surface structure of CsSnI_3 , *ACS Appl. Mater. Interfaces* 12 (10) (2020) 12353–12361, <https://doi.org/10.1021/acsami.9b22967>.
- [70] J. Zhang, J. Qin, T. Wu, B. Hu, Doping induced orbit-orbit interaction between excitons while enhancing photovoltaic performance in tin perovskite solar cells, *J. Phys. Chem. Lett.* 11 (17) (2020) 6996–7001, <https://doi.org/10.1021/acs.jpclett.0c01859>.
- [71] W. Li, J. Li, J. Li, J. Fan, Y. Mai, L. Wang, Additive-assisted construction of all-inorganic CsSnI_3 2 mesoscopic perovskite solar cells with superior thermal stability up to 473 K, *J. Mater. Chem. A* 4 (43) (2016) 17104–17110, <https://doi.org/10.1039/C6TA08332C>.
- [72] T.-B. Song, T. Yokoyama, C.C. Stoumpos, J. Logsdon, D.H. Cao, M.R. Wasielewski, S. Aramaki, M.G. Kanatzidis, Importance of reducing vapor atmosphere in the fabrication of tin-based perovskite solar cells, *J. Am. Chem. Soc.* 139 (2) (2017) 836–842, <https://doi.org/10.1021/jacs.6b10734>.
- [73] E. Jokar, C.-H. Chien, A. Fathi, M. Rameez, Y.-H. Chang, E.-W.-G. Diau, Slow surface passivation and crystal relaxation with additives to improve device performance and durability for tin-based perovskite solar cells, *Energy Environ. Sci.* 11 (9) (2018) 2353–2362, <https://doi.org/10.1039/C8EE00956B>.
- [74] M. Chen, G. Kapil, Y. Li, M.A. Kamarudin, A.K. Baranwal, K. Nishimura, S. Rahamir, Y. Sanechira, H. Li, C. Ding, Z. Zhang, Q. Shen, S. Hayase, Large synergy effects of doping, a site substitution, and surface passivation in wide bandgap Pb-free ASn_2Br perovskite solar cells on efficiency and stability enhancement, *J. Power Sources* 520 (2022), 230848, <https://doi.org/10.1016/j.jpowsour.2021.230848>.
- [75] H. Wu, Y. Wang, A. Liu, J. Wang, B.J. Kim, Y. Liu, Y. Fang, X. Zhang, G. Boschloo, E.M. Johansson, Methylammonium bromide assisted crystallization for enhanced lead-free double perovskite photovoltaic performance, *Adv. Funct. Mater.* 32 (14) (2022) 2109402, <https://doi.org/10.1002/adfm.202109402>.
- [76] K.M. Boopathi, P. Karuppuswamy, A. Singh, C. Hanmandlu, L. Lin, S.A. Abbas, C. Chang, P.C. Wang, G. Li, C.W. Chu, Solution-processable antimony-based light-absorbing materials beyond lead halide perovskites, *J. Mater. Chem. A* 5 (39) (2017) 20843–20850, <https://doi.org/10.1039/C7TA06679A>.
- [77] F. Umar, J. Zhang, Z. Jin, I. Muhammad, X. Yang, H. Deng, K. Jahangeer, Q. Hu, H. Song, J. Tang, Dimensionality controlling of $\text{Cs}_3\text{Sb}_2\text{I}_9$ for efficient all-inorganic planar thin film solar cells by HCl-assisted solution method, *Adv. Opt. Mater.* 7 (5) (2019) 1801368, <https://doi.org/10.1002/adom.201801368>.
- [78] P. Karuppuswamy, K.M. Boopathi, A. Mohapatra, H.-C. Chen, K.-T. Wong, P.-C. Wang, C.-W. Chu, Role of a hydrophobic scaffold in controlling the crystallization of methylammonium antimony iodide for efficient lead-free perovskite solar cells, *Nano Energy* 45 (2018) 330–336, <https://doi.org/10.1016/j.nanoen.2017.12.051>.
- [79] A. Singh, S. Najman, A. Mohapatra, Y.-J. Lu, C. Hanmandlu, C.-W. Pao, Y.-F. Chen, C.S. Lai, C.-W. Chu, Modulating performance and stability of inorganic lead-free perovskite solar cells via lewis-pair mediation, *ACS Appl. Mater. Interfaces* 12 (29) (2020) 32649–32657, <https://doi.org/10.1021/acsami.0c06971>.
- [80] J. Li, Y. Lv, H. Han, J. Xu, J. Yao, Two-dimensional $\text{Cs}_3\text{Sb}_2\text{I}_{9-x}\text{Cl}_x$ Film with (201) preferred orientation for efficient perovskite solar cells, *Materials* 15 (8) (2022) 2883, <https://doi.org/10.3390/ma15082883>.
- [81] A. Singh, P.-T. Lai, A. Mohapatra, C.-Y. Chen, H.-W. Lin, Y.-J. Lu, C.-W. Chu, Panchromatic heterojunction solar cells for Pb-free all-inorganic antimony based perovskite, *Chem. Eng. J.* 419 (2021), 129424, <https://doi.org/10.1016/j.cej.2021.129424>.
- [82] Y. Yang, C. Liu, M. Cai, Y. Liao, Y. Ding, S. Ma, X. Liu, M. Guli, S. Dai, M. K. Nazeeruddin, Dimension-controlled growth of antimony-based perovskite-like halides for lead-free and semitransparent photovoltaics, *ACS Appl. Mater. Interfaces* 12 (14) (2020) 17062–17069, <https://doi.org/10.1021/acsami.0c00681>.
- [83] X. Yang, Y. Chen, P. Liu, H. Xiang, W. Wang, R. Ran, W. Zhou, Z. Shao, Simultaneous power conversion efficiency and stability enhancement of $\text{Cs}_2\text{AgBiBr}_6$ 6 lead-free inorganic perovskite solar cell through adopting a multifunctional dye interlayer, *Adv. Funct. Mater.* 30 (23) (2020) 2001557, <https://doi.org/10.1002/adfm.202001557>.
- [84] Z. Zhang, C. Wu, D. Wang, Q. Zhang, Y. Zhang, X. Guo, Y. Lao, B. Qu, L. Xiao, Z. Chen, Efficient nonlead double perovskite solar cell with multiple hole transport layers, *ACS Appl. Energy Mater.* 3 (10) (2020) 9594–9599, <https://doi.org/10.1021/acsami.0c01066>.
- [85] B. Wang, L. Yang, C. Dall'Agnese, A.K. Jena, S.-I. Sasaki, T. Miyasaka, H. Tamiaki, X.-F. Wang, Photoactive Zn-chlorophyll hole transporter-sensitized lead-free $\text{Cs}_2\text{AgBiBr}_6$ perovskite solar cells, *Sol. RRL* 4 (7) (2020) 2000166, <https://doi.org/10.1002/solr.202000166>.
- [86] M.T. Sirtl, R. Hooijer, M. Armer, F.G. Ebadi, M. Mohammadi, C. Maheu, A. Weis, B. T. van Gorkom, S. Häringer, R.A.J. Janssen, T. Mayer, V. Dyakonov, W. Tress, T. Bein, 2D/3D hybrid $\text{Cs}_2\text{AgBiBr}_6$ double perovskite solar cells: improved energy

- level alignment for higher contact-selectivity and large open circuit voltage, *Adv. Energy Mater.* 12 (7) (2022) 2103215.
- [87] A. Hiltunen, N. Lamminen, H. Salonen, M. Liu, P. Vivo, Efficiency improvement for perovskite-inspired Cs₃Sb₂I₉ solar cells using P3HT as the hole transport material, *Sustain. Energy Fuels* 6 (1) (2022) 217–222, <https://doi.org/10.1039/D1SE01150B>.
- [88] W. Hu, X. He, Z. Fang, W. Lian, Y. Shang, X. Li, W. Zhou, M. Zhang, T. Chen, Y. Lu, L. Zhang, L. Ding, S. Yang, Bulk heterojunction gifts bismuth-based lead-free perovskite solar cells with record efficiency, *Nano Energy* 68 (2020), 104362, <https://doi.org/10.1016/j.nanoen.2019.104362>.
- [89] G. Paul, A.J. Pal, Impact of band-engineered polymer-interlayers on heterojunction solar cells based on 2D-layered perovskites (Cs₃Sb₂Cl_xI_{9-x}), *Sol. Energy* 232 (2022) 196–203, <https://doi.org/10.1016/j.solener.2021.12.056>.
- [90] M. Liu, H. Pasanen, H. Ali-Löytty, A. Hiltunen, K. Lahtonen, S. Qudsia, J.H. Smått, M. Valden, N.V. Tkachenko, P. Vivo, B-Site co-alloying with germanium improves the efficiency and stability of all-inorganic tin-based perovskite nanocrystal solar cells, *Angew. Chem. Int. Ed.* 59 (49) (2020) 22117–22125, <https://doi.org/10.1002/ange.202008724>.
- [91] T. Luo, Y. Zhang, X. Chang, J. Fang, T. Niu, J. Lu, Y. Fan, Z. Ding, K. Zhao, S.F. Liu, Dual interfacial engineering for efficient Cs₂Ag₃BiBr₆ based solar cells, *J. Energy Chem.* 53 (2021) 372–378, <https://doi.org/10.1016/j.jechem.2020.05.016>.
- [92] Z. Zhao, F. Gu, Y. Li, W. Sun, S. Ye, H. Rao, Z. Liu, Z. Bian, C. Huang, Mixed-organic-cation tin iodide for lead-free perovskite solar cells with an efficiency of 8.12%, *Adv. Sci.* 4 (11) (2017) 1700204, <https://doi.org/10.1002/advs.201700204>.